

# Magneto-Optical Trap Based Multi-directional Cold Atomic Fountain

by

Itamar SIVAN

Stage long de recherche, FIP M1

in the

Department of Physics  
University of Oxford

under the supervision of

Dr. Axel Kuhn

August 2010

## Abstract

Employing a hybrid of optical and magnetic fields, one can produce a magneto-optical trap (MOT), a configuration where atoms are strongly confined and cooled down to low temperatures. In the presence of counter-propagating optical fields, a uniform magnetic field, inducing a Zeeman-split of the atomic levels, can give rise to damping to different resonant velocities, resulting in a moving optical molasses. These velocities are governed by the magnitude of the Larmor frequency,  $v_r = n \cdot \omega_L / K$ , with the five possible velocity groups  $n = 0, \pm 1, \pm 2$ . Each of the velocity groups is attributed to a coherent two-photon velocity-selective resonance between atomic ground-state sub-levels. We have realised a  $^{87}\text{Rb}$  magneto-optical trap and an optical molasses showing kinetic temperatures in the sub-Doppler regime, using an injection-locked diode laser. Utilising the MOT as a source for cold atoms, we have demonstrated a multi-directional atomic fountain, namely, three moving optical molasses simultaneously propagating in three different directions. The extracted atomic fountains show both longitudinal and transversal temperatures in the sub-Doppler regime. We characterize the fountains' motion for it to be used in a realisation of a quantum computation execution proposal. It shall be used for the insertion of single atoms into micro-scale optical cavities.

En utilisant un hybride de champs laser et magnétique, on peut produire un piège magnéto optique, une configuration dans laquelle les atomes sont fortement confinés et refroidis à de très basses températures. En présence de champs laser contre propagatifs, un champ magnétique uniforme, induisant l'effet Zeeman sur les niveaux atomiques, peut entraîner un amortissement à des vitesses résonnantes, mettant en évidence une mélasse optique dynamique. Les vitesses sont gouvernées par l'amplitude de la fréquence de Larmor  $v_r = n \cdot \omega_L / K$ , avec les cinq groupes de vitesses possible  $n = 0, \pm 1, \pm 2$ . Chacune de celles ci est attribuée à une vitesse-sélective transition cohérente à deux photons. On a réalisé un piège magnéto-optique et une mélasse optique ayant des températures dans le régime sub-Doppler, en utilisant une diode laser à verrouillage d'injection. En exploitant le MOT en tant que source d'atomes froids, on a démontré une fontaine atomique multi-directionnelle, c'est-à-dire, trois mélasses optiques se propageant simultanément dans trois directions différentes. La fontaine ainsi créée montre des températures longitudinale et transversale dans le régime sub-Doppler. On a caractérisé son mouvement afin qu'elle serve pour l'exécution d'une proposition en information quantique. Elle sera utilisée pour l'insertion d'atomes uniques dans des cavités optiques d'échelle microscopique.

# Contents

<b>1</b>	<b>Motivation</b>	<b>1</b>
1.1	Quantum information . . . . .	1
1.2	Towards a scalable quantum network . . . . .	1
1.3	Putting an atom inside a cavity . . . . .	3
<b>2</b>	<b>Introduction</b>	<b>4</b>
2.1	Optical molasses . . . . .	4
2.2	Magneto-optical trap . . . . .	6
2.3	Sub-doppler laser cooling . . . . .	7
<b>3</b>	<b>Experimental setup</b>	<b>8</b>
3.1	Apparatus . . . . .	8
3.1.1	Injection locking . . . . .	11
3.2	System control . . . . .	12
<b>4</b>	<b>The trap</b>	<b>12</b>
4.1	Loading measurements . . . . .	12
4.2	Temperature measurements . . . . .	13
4.2.1	Optical depth . . . . .	13
4.2.2	Time-of-flight . . . . .	13
<b>5</b>	<b>Atomic fountain</b>	<b>16</b>
5.1	Moving molasses . . . . .	16
5.2	3D configuration . . . . .	17
5.3	Observations . . . . .	20
5.3.1	Three atomic fountains . . . . .	20
5.3.2	Single atomic fountain . . . . .	21
5.3.3	Interaction time . . . . .	22
<b>6</b>	<b>Achievements</b>	<b>25</b>
<b>A</b>	<b>Pound-Drever-Hall</b>	<b>26</b>
<b>B</b>	<b>Helmholtz coils</b>	<b>26</b>
<b>C</b>	<b>Experimental setup</b>	<b>27</b>
<b>D</b>	<b>Numerical solution</b>	<b>28</b>

# Acknowledgements

I would like to thank Dr. Axel Kuhn for inviting me to undertake this project within his research group, the atom-photon-connection. The project was a very stimulating and inspiring experience, and I am very grateful for this opportunity. I am also very grateful for all the advice and orientation that were without a doubt extremely helpful.

I would also like to thank Jerome Dille and Dr. Matt Himsforth for their enormous help and good will, Peter Nisbet for the help, the good will, and the very stimulating discussions and Lukas Brandt, Cecilia Muldoon, Gunnar Langfahl-Klabes and Jian Dong, for many enriching advice and for the pleasant and inspiring atmosphere.

## 1 Motivation

### 1.1 Quantum information

The project is inscribed in the context of quantum information. At the present time quantum computers are mostly theoretical constructs but nevertheless, it has been proved that in many cases the quantum algorithms are faster than the classical ones by far [12,13,16,17,35]. Since the information carriers are treated in a frame where particles can be in a superposition of several states, quantum algorithms allow us to go beyond the standard 0/1 bit, introducing the quantum-bit:

$$|\psi\rangle = \alpha|0\rangle + \beta|1\rangle \quad (1)$$

Being in a superposition allows the qubit to undergo an algorithm as a 0 bit and a 1 bit in the same time, with the respective amplitudes; in other terms, a qubit undergoing an algorithm is in a way equivalent to two classical bits undergoing it. Furthermore, qubits can be entangled, and produce Bell states.

A good example for these two substantial features arises from the Deutsch-Jozsa quantum algorithm [12,13]. The task is to determine whether a function  $f: \{0,1\}^n \rightarrow \{0,1\}$  is constant or balanced<sup>1</sup>, given that it is surely one of them. The classical algorithm is straight-forward and consists on evaluating the function for different combinations of  $n$  bits. Clearly, in the worst case,  $2^{n-1} + 1$  evaluations are required. On the other hand, the Deutsch-Jozsa quantum algorithm requires only a single query of  $f$  providing us with a deterministic result. The input of Deutsch-Jozsa algorithm is an entangled state of  $n$  qubits, each in a superposition as denoted in equation 1.

In terms of efficiency, the two most famous quantum algorithms are Grover's algorithm [16, 17] and Shor's algorithm [35]. The first is the quantum algorithm for searching an unsorted database with  $N$  entries and scales in time as  $O(N^{1/2})$ , while the classical algorithm scales as  $O(N)$ . The second is the quantum algorithm for integer factorization and runs in polynomial time  $O((\log N)^3)$ , which is exponentially faster than the classical algorithm that scales as  $O(e^{(\log N)^{1/3} \cdot (\log \log N)^{2/3}})$ .

### 1.2 Towards a scalable quantum network

Many suggestions for the execution of quantum algorithms have been made. Furthermore, quantum bits and/or gates were already implemented using several different techniques:

---

<sup>1</sup>A constant function returns 0 or 1 for all inputs while a balanced function returns 1 for half of the inputs in the domain and 0 for the other half

single-photons sources as molecules [5, 11, 24], semiconductor quantum dots [27, 33, 42] or trapped ions [6], superconducting quantum interference devices (SQUIDS) [29], nuclear magnetic resonance (NMR) [9], etc. Nevertheless, the passage from a single quantum gate or an entanglement of several qubits to a scalable system, capable of executing algorithms, has, for the time being, not been achieved. The common ground of all the suggested schemes is the aim to arbitrarily address, manipulate, and couple qubits. The goal of the research within the atom-photon-connection research group is to demonstrate a system where these are achievable to a high level of control, by interfacing single atoms and single photons. The execution of quantum algorithms in this context is hence fundamentally based on the interactions of atoms and photons on the single-atom and single-photon level. We wish to demonstrate a fully characterized deterministic sources of indistinguishable qubits, which is the key element for quantum information processing. The sources, neutral atoms, will then act as quantum gates and quantum memories, while the qubits, photons, as information carriers, creating entanglement and teleporting quantum states.

Single neutral atoms, strongly coupled to a high-finesse optical cavity<sup>2</sup> and exposed to a classical laser field can emit and absorb single photons on demand. These photons will be emitted into the cavity mode, and then leave the cavity through one of the mirror which is set with a slightly lower reflectivity coefficient.

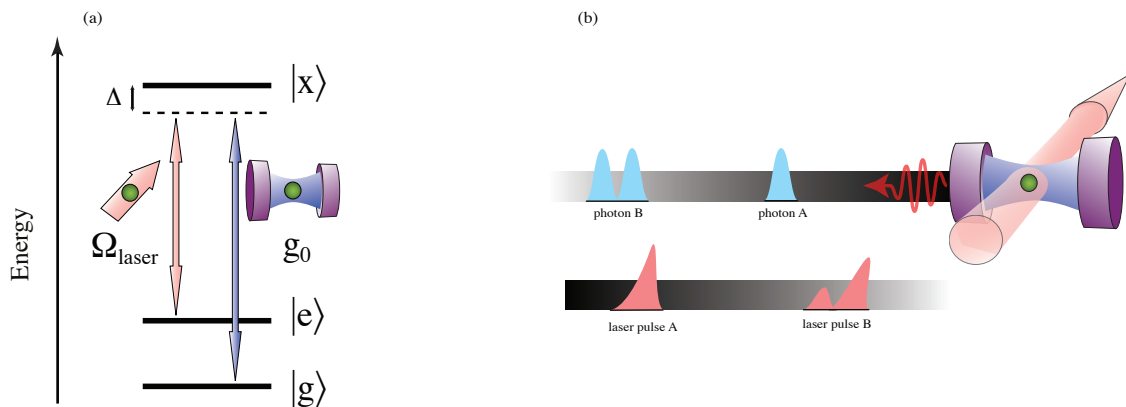


Figure 1: (a) A three-state level structure, coupled to a laser field and a high-finesse optical cavity. The atom can undergo a direct passage between the two ground states  $|e\rangle$  and  $|g\rangle$ . (b) An illustration of the process. The temporal shape of the laser-pulse determines that of the emitted photon. Implemented in a quantum network, this photon will then be absorbed by a second atom in a second cavity. It is hence substantial that the photon has a symmetric shape so that it is seen by the emitter and absorber in the same way. We show typical laser-pulse shapes that result in symmetric photon shapes [21].

In order to understand how single atoms can do so, we consider the three-states level structure in figure 1 (a). The first dipole transition  $|e\rangle \leftrightarrow |x\rangle$  is coupled to the laser field through the Rabi frequency:

$$\Omega(t) = \left| \hat{\mathbf{d}} \cdot \mathbf{E}(t) \right| / \hbar \quad (2)$$

where  $\hat{\mathbf{d}} = e\hat{\mathbf{r}}$  is the atomic dipole moment operator for the corresponding transition, with  $\hat{\mathbf{r}}$  being the corresponding effective position of the electron with respect to the nucleus, and  $\mathbf{E}(t)$  is the light's electric field in the dipole approximation<sup>3</sup>. The second dipole transition

<sup>2</sup>The finesse is the ratio of the free spectral range of an optical resonator by its bandwidth. It represents how well light is confined in the cavity, and for a reflectivity coefficient  $R > 0.5$  it is approximately an increasing function of  $R$  solely.

<sup>3</sup>The dipole approximation is valid as long as the wavelength of the light is significantly greater than the

$|e\rangle \leftrightarrow |g\rangle$  is strongly coupled to the optical cavity through the atom-cavity coupling constant  $g_0$ . The coupling is given by the Hamiltonian:

$$H_{int}(t) = \hbar \left[ \Delta_L |e\rangle \langle e| + \Delta_C |g\rangle \langle g| - \frac{\Omega(t)}{2} (|x\rangle \langle e| + |x\rangle \langle e|) - g_0 (|x\rangle \langle g| \hat{a} + \hat{a}^\dagger |g\rangle \langle x|) \right] \quad (3)$$

where  $\Delta_L$  and  $\Delta_C$  are the detunings from resonance of the laser and the cavity fields respectively, each with its corresponding transition.

If an atom enters the cavity while in the  $|e\rangle$  state, it can be pumped directly <sup>4</sup> into the  $|g\rangle$  state, namely, undergoing a stimulated adiabatic Raman passage (STIRAP) [22]. That consists on the absorption of a photon from the laser field and the emission of another into the cavity mode. Furthermore, the temporal shape of the emitted photon follows the probability of occupation of the  $|g\rangle$  state, since,  $\rho_{gg}(t) \propto |\Psi_{photon}(t)|^2$ . This relation arises from the last term in equation 3; the photon is emitted to the cavity mode when the atom undergoes the transition  $|g\rangle \rightarrow |x\rangle$ . Hence, it follows the solution of the density matrix evolution equation:

$$\dot{\hat{\rho}}(t) = \frac{1}{i\hbar} [\hat{H}, \hat{\rho}(t)] + \hat{L}\hat{\rho} \quad (4)$$

where  $\hat{L}$  is the Liouville operator, accounting for the spontaneous decay of the atom and the cavity. The variables in that equation, using the Hamiltonian in equation 3, are the detunings and the Rabi frequency, which can be a function of time. Determining those, determines the evolution of the density matrix. Furthermore, it was shown [21] that this process can be analytically inverted : we can choose the desired temporal form of  $|\Psi(t)_{photon}|^2$ , and resolve the required detuning and function  $\Omega(t)$ . That will allow us to produce photons of arbitrary shapes, and most importantly symmetric ones.

The coherence properties of the transition are uniquely determined by the parameters of the cavity, namely, by the Purcell factor [31], and the driving process. Hence, different cavities can produce indistinguishable photons, in a well-defined mode, with a symmetric temporal line-shape. These characteristics make these emitted photons suitable to act as quantum-bits and the described proposal promising as a milestone towards a scalable quantum network.

### 1.3 Putting an atom inside a cavity

In order to undergo a STIRAP process, an atom must be within a cavity for a duration of 10  $\mu s$ . It was demonstrated [20] that a STIRAP process can be performed using a cold atomic cloud, free-falling from a magneto-optical trap, passing through a cavity for a duration of 20  $\mu s$ . This allows us to avoid the experimental difficulties of the integration of micro-scale traps, as Paul and Penning traps, within the optical cavity. For the extraction of low-velocity cold atomic fountains from MOTs both intensity imbalance [18, 25] and frequency imbalance [2, 3, 7, 15, 40] of the laser fields propagating from above and below an atomic cloud have been employed. Frequency imbalance can be achieved either by shifting the frequency of the lasers [2, 7] or by Zeeman-shifting the atomic levels [3, 15, 40]. While most commonly quantum optics experiments exploit laser frequency shifting using optical modulators, in this project we utilise the Zeeman-shift due to a uniform magnetic field. This method is more robust and less expensive by far, as it consists on a pair of Helmholtz coils solely and avoids the use of many optical instruments. We demonstrate a new feature of simultaneously extracting three

---

atom so that the field is spatially slowly-varying and we assume that it is constant in the whole interaction region

<sup>4</sup>Keeping the occupation of  $|x\rangle$  zero. Referred to as a 'dark' state.

atomic fountains from the magneto-optical trap, propagating in different directions, as seen in images 20 and 15. This feature can be used for simultaneous insertion of single atoms into up to three optical cavities.

The modes of the cavity are naturally not constant within it. In fact, the atom-cavity coupling constant  $g_0$  is to be used only if we consider maximum coupling, when the atom is static in anti-node of the cavity mode. Since this is not the case if we consider an atom ballistically moving inside the cavity, we are to replace  $g_0$  in equation 3 by  $g(\mathbf{r}) = g_0 \Psi_{cavity}(\mathbf{r})$ , where  $\Psi_{cavity}(\mathbf{r})$  is the cavity mode spatial shape, taken in the time-dependent location of the atom  $r(t)$ . Naturally, it arises that we need good control of the atoms'. Therefore, after demonstrating the multi-directional atomic fountain, an emphasis is put on the characterization of its motion.

## 2 Introduction

### 2.1 Optical molasses

Optical molasses is a laser cooling technique used in order to cool down neutral atoms [26]. The technique consists on three pairs of counter-propagating beams, situated along three perpendicular axes. Cooling down atoms is very significant in quantum mechanics not only because many phenomena occur at very low temperatures but also because it provides us with a tool for the study of individual atoms<sup>5</sup>. The temperature of the atoms is defined by the standard deviation of the Maxwell-Boltzmann distribution of their energy:

$$p(v) = \sqrt{\frac{m}{2\pi k_B T}} e^{-\frac{m(v-v_0)^2}{2k_B T}} \quad (5)$$

From that relation it is clear that by definition, narrowing the distribution in energy is cooling down the atoms. Furthermore, when the distribution is centered around  $v_0 = 0$ , then decreasing the mean velocity  $\langle v \rangle = \sqrt{k_B T/m}$  is interpreted as cooling as well. A one-dimension schematic of the cooling process is shown in figure 2.

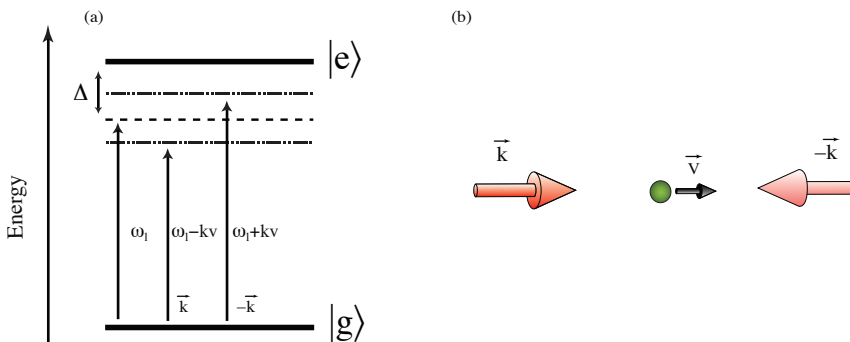


Figure 2: (a) A simple two-state level structure. The laser frequency  $\omega_l$  is red detuned from resonance with the atomic transition. The separation of the apparent detunings of the lasers results in a force of friction since the closer is a laser frequency to resonance, the stronger is the radiation pressure. It is only for  $\mathbf{v} = 0$  that the radiation pressure is isotropic. (b) Illustration of a 1D configuration; an atom within a pair of counter-propagating laser fields.

The two counter-propagating beams are seen by the moving atom with different apparent frequencies due to the Doppler shift:  $\omega_i = \omega_l - \mathbf{k}_i \cdot \mathbf{v}$ , where  $\omega_i$  is the apparent frequency

<sup>5</sup>In fact, laser cooling techniques were demonstrated as well with molecules and microscopic beads and is a useful tool in the investigations of chemical reactions.

in the atom's frame,  $\omega_l$  the frequency in the laboratory frame and  $\mathbf{k}_i$  the wave vector in the laboratory frame. As a result, if the frequency is slightly detuned below resonance, the moving atom sees the light it moves towards Doppler-shifted closer to resonance, whereas the light it moves away from is shifted away from resonance. Since the closer a light field is to resonance, the stronger is its radiation pressure, this results in the damping of the atom's velocity.

In order to deduce the resultant damping force we regard it as the result of the difference in momentum between each absorbed photon and the emitted one that follows,  $\Delta\mathbf{p} = \hbar\mathbf{k}_{abs} - \hbar\mathbf{k}_{emit}$ . The direction of spontaneous emission, and hence of  $\hbar\mathbf{k}_{emit}$ , is random, while for a single light beam all  $\hbar\mathbf{k}_{abs}$  are pointing in the direction of propagation. Thus, if we sum over a large number of momentum kicks, all  $\hbar\mathbf{k}_{emit}$ 's will cancel out and we are left with  $\langle\Delta\mathbf{p}\rangle = \hbar\mathbf{k}$ , with  $\mathbf{k}$  being the wave-vector of the light beam. Now the force of a single light field, being the rate of change of momentum, can be expressed as:

$$\mathbf{F} = \hbar\mathbf{k}R_{scatt} \quad (6)$$

where  $R_{scatt} = \rho_{ee}\Gamma$  is the scattering rate, with  $\Gamma$  the rate of spontaneous emission and  $\rho_{ee}$  the steady-state probability of occupying the excited level.  $\rho_{ee}$  is obtained by solving the density matrix evolution equation 4 for the steady state, using the following Hamiltonian:

$$\hat{H}(t) = \hbar\omega_0 (|e\rangle\langle e|) + \hat{\mathbf{d}} \cdot \mathbf{E}(t) \quad (7)$$

where the first term is the non-perturbed Hamiltonian  $H_0$  and the second stands for the atom-field coupling. The solution to that equation leads us to the expression:

$$\mathbf{F} = \hbar\mathbf{k} \frac{\Gamma}{2} \frac{\Omega^2/2}{\delta^2 + \Omega^2/2 + \Gamma^2/4} \quad (8)$$

where

$$\delta = \omega_l - (\omega_0 - \mathbf{k} \cdot \mathbf{v}) \quad (9)$$

is the effective detuning of the laser field from the atomic resonance, taking into account the Doppler shift. The force in equation 8 is the fundamental expression for radiation pressure, following a Lorentzian shape. In figure 3 we show the eventual force that arises from the addition of the forces of a pair of counter-propagating laser beams which is the eventual force exerted on an atom in a 1D optical molasses:

$$\mathbf{F} = \mathbf{F}(\omega_l - (\omega_0 - \mathbf{k} \cdot \mathbf{v})) + \mathbf{F}(\omega_l - (\omega_0 + \mathbf{k} \cdot \mathbf{v})) \quad (10)$$

For low velocities,  $kv \ll \Gamma$ , equation 10 can be approximated to:

$$F = -2 \frac{\partial F}{\partial \omega} kv = -M \left[ 4\hbar k^2 \frac{I}{I_{sat}} \frac{-2\Delta/M\Gamma}{[1 + (2\Delta/\Gamma)^2]^2} \right] v \quad (11)$$

where  $\Delta = \omega_l - \omega_0$  and we define the saturation intensity as  $I/I_{sat} = 2\Omega^2/\Gamma^2$ . We see that it is only for negative detunings  $\Delta < 0$  that the optical molasses results in damping  $F = -M\gamma v$  with  $\gamma = \gamma(\delta, I)$ . The low-velocities approximation is valid for velocities  $v \ll 5 \frac{m}{s}$ , with  $\Gamma = 2\pi \cdot 6.1 \cdot 10^6 s^{-1}$  and  $\lambda \cong 780$  for the  $^{87}Rb$  ( $5^2S_{1/2} \rightarrow 5^2P_{3/2}$ ) transition, seen in figure 6.

In the regime where the recoil velocity  $v_R = \hbar k/m$ , defined by the momentum jumps that the atom suffers, is much smaller than the width of its momentum distribution, the optical molasses can be described by the Fokker-Planck equation [38]. Then the temperature can be deduced from the Einstein relation  $k_B T = D/\gamma$ , where  $D$  is the diffusion coefficient.

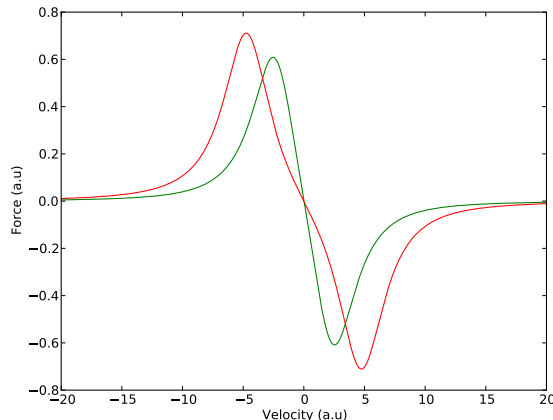


Figure 3: The force of friction in the optical molasses technique as a function of velocity. Around  $v = 0$  the force can be expressed in the form  $F = -M\gamma v$ . The slope depends upon the intensity of the field and the detuning. In green is the force for  $\delta = -\Gamma/2$ , in red for  $\delta = -\Gamma$

Following that equation, we find that the minimal temperature that can be reached for this configuration occurs at non-saturating intensities and at a light frequency that is below resonance by about  $-\Gamma/2$ . This minimal value, called the Doppler limit, is given by [23, 41]:

$$k_B T_D = \hbar\Gamma/2 \quad (12)$$

which corresponds in our case to  $146\mu K$ .

## 2.2 Magneto-optical trap

We confine the atoms into a small region using a magneto-optical trap (MOT) set-up [26]. The MOT is a very robust trap and is probably the easiest and least expensive way of producing atomic samples below  $1\text{ mK}$ . The trap consists on a pair of anti-Helmholtz coils and three pairs of orthogonal counter-propagating laser beams, as illustrated in figure 4(b).

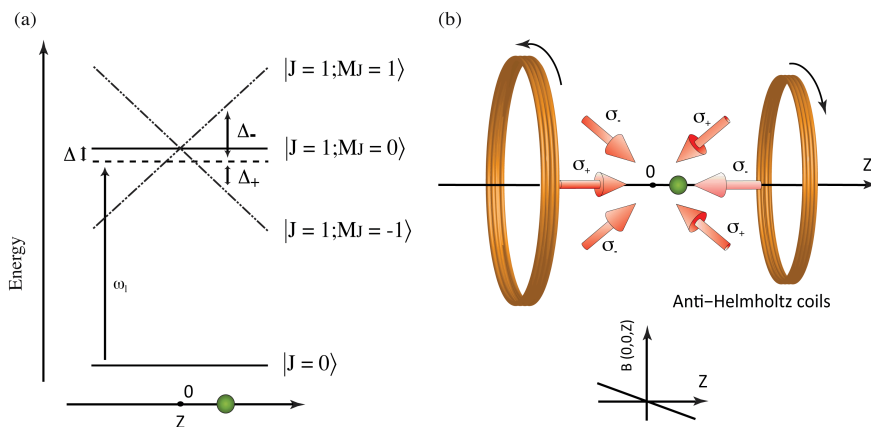


Figure 4: (a) The level structure in the presence of a space-dependent magnetic field of constant gradient. We note  $\Delta_-$  ( $\Delta_+$ ) as the effective detuning of the laser propagating to the right (left). Those are equal only for  $z = 0$ . Note that the scales do not coincide with the utilized parameters since in fact the Zeeman energy split is much smaller than the optical transition energy. (b) The magneto-optical trap configuration. Whenever the atom moves from the center of the trap, an imbalance of the radiation pressure of the two counter-propagating laser beams is induced, and it is restored to center.

The beams are set similarly to the optical molasses technique, only that along each axis, one beam is set to be right-circularly polarized, denoted  $\sigma_+$ , and the other left-circularly polarized, denoted  $\sigma_-$ <sup>6</sup>. In other terms, the first light field contains photons with spin  $|+1\rangle_z$  and the second contains photons with spin  $|-1\rangle_z$ , where  $\hat{z}$  is parallel to the direction of propagation of the first. As a result, the  $\sigma_+$  and  $\sigma_-$  light fields are coupled only to dipole transitions between states which are separated by an angular-momentum  $\Delta M_J = +1$  and  $\Delta M_J = -1$  respectively. The magnetic field along the  $z$  axis, shown in figure 4(b), is assumed to have a constant gradient<sup>7</sup> and leads to a space-dependent Zeeman split, shown in figure 4(b). Consequently, if an atom is to the right of the zero-point of the magnetic field, the laser field propagating from right to left is 'Zeeman-shifted' closer to resonance with the transition to which it is coupled  $|J = 0\rangle \Rightarrow |J = 1; M_J = -1\rangle$  than the laser field propagating from left to right with the corresponding transition. Namely, if the atom is to the right of the zero-point of the magnetic field, an imbalance in the detunings is induced,  $\Delta_- < \Delta_+$ , and hence an imbalance in the radiation pressure, and it is restored. The radiation pressure of the two counter-propagating beams is equal only for  $z = 0$ .

Thus the magneto-optical trap configuration creates a restoring force, on top of the damping force explained in section 2.1. Quantitatively, we can add the coupling to the magnetic field to the Hamiltonian in equation 7:

$$\begin{aligned} \hat{H}(t) = & \hbar\omega_0 (|J = 1\rangle \langle J = 1|) + \hat{\mathbf{d}} \cdot \mathbf{E}(t) \\ & + \hbar\omega_L (|J = 1; M_J = +1\rangle \langle J = 1; M_J = -1| - |J = 1; M_J = -1\rangle \langle J = 1; M_J = +1|) \end{aligned}$$

where  $|J\rangle = |J = 1; M_J = +1\rangle + |J = 1; M_J = 0\rangle + |J = 1; M_J = -1\rangle$  and  $\omega_L = g_J \mu_B B / \hbar$  is the Larmor frequency, with  $g_J$  the Landé factor and  $\mu_B$  Bohr's magneton. We clearly see that we can replace  $\omega_0$  in equation 9 by  $\omega_0 + \omega_L$  and  $\omega_0 - \omega_L$  for the transition driven by the  $\sigma^-$  and  $\sigma^+$  laser field respectively. We conclude that the force on an atom within a magneto-optical trap can be regarded as a result of the space-velocity dependence of the detuning of a laser field from the transition to which it is coupled:

$$\delta^{\sigma^\pm}(z, v) = \omega_l - (\omega_0 \pm \omega'_L z \pm kv) \quad (13)$$

and

$$\mathbf{F} = \mathbf{F}(\omega_l - (\omega_0 - \omega'_L z - \mathbf{k} \cdot \mathbf{v})) + \mathbf{F}(\omega_l - (\omega_0 + \omega'_L z + \mathbf{k} \cdot \mathbf{v})) \quad (14)$$

where we defined  $\omega'_L z = \omega_L$ , and with  $B = \frac{dB}{dz} z$  (see foot-note 7) we get  $\omega'_L = \frac{g_J \mu_B}{\hbar} \cdot \frac{dB}{dz}$ . For Zeeman shifts  $\omega_L \ll \Gamma$  we can approximate the force as we did for the optical molasses. This results in:

$$F = -M\gamma \cdot v - \frac{M\gamma\omega'_L}{k} \cdot z \quad (15)$$

Hence, the force within the magneto-optical trap is both damping, with the friction coefficient  $\gamma$ , and restoring, with a spring constant  $M\gamma\omega'_L/k$ .

### 2.3 Sub-doppler laser cooling

Temperatures lower than the Doppler limit can be achieved if we consider the multiplicity of the ground state, following the model introduced J. Dalibard and C. Cohen-Tannoudji [10]. The substantial ingredient to the enhancement of the damping force is the variation of the

<sup>6</sup>The rotation of the field is defined with respect to the axis of the laser-beams pair

<sup>7</sup>The field can be considered linear on the scale of the trap, where  $r_{MOT} \ll r_{coils}$

relative orientation of the atomic dipole moment with respect to the light polarization while traveling through a wave length. That is the case when the atom encounters a field with a polarization gradient. In the configuration that we use, shown in figure 4, which consists on a pair of counter-propagating laser fields with circular but orthogonal polarizations, the electric field has a constant magnitude and is linearly polarized everywhere, but its direction undergoes a rotation of  $2\pi$  over one wavelength. If we consider the quantization axis as the direction of the local polarization vector  $\hat{n}$ , then the sub-states of a stationary atom in the light field will be redistributed in a way that the  $|F = 1, m_F = 0\rangle_n$  will be populated most strongly, if we consider an  $|F = 1\rangle$  to  $|F = 2\rangle$  dipole transition. Then, when the atom moves, the electric field rotates. If we then consider the new direction of the electric field  $\hat{n}'$  as quantization axis, the ground-state sub-levels are mixed and the light field attempts to redistribute the population again into the steady state, where  $|F = 1, m_F = 0\rangle_{n'}$  is populated most strongly. Since the dipole moment follows the polarization direction non-adiabatically, it does not reach the steady-state population during his motion. It was shown [10] that as a result, an atom scatters photons much more efficiently from the laser field towards it is moving. This results in a damping force which is of a different nature then the Doppler force, attributed to the time lag in the following of the atomic dipole orientation of the local electric field.

### 3 Experimental setup

#### 3.1 Apparatus

In figure 5 is a full schematic of the experimental setup, as it is at the end of the project.

The left side contains the lasers and the used optical instruments, while the right side shows the vacuum chamber, where the magneto-optical trap and the atomic fountain are situated. The coils situated on the sides of the vacuum chamber are a pair of anti-Helmholtz coils, creating a linearly-inhomogeneous magnetic field in its center, are used for the MOT. The coils situated above and below the vacuum chamber are a pair of Helmholtz coils, creating a uniform magnetic field in its center, used for the extraction of the atomic fountain. We made the Helmholtz coils for this purpose, and an emphasis was put on the homogeneity of the magnetic field in the center of the chamber, and on lowering their switching times. Switching times are measured to be  $55 \mu s$ , as shown in appendix B. Images of the setup are shown in appendix C.

In figure 6 we show the  $5^2S_{1/2}$  and  $5^2P_{3/2}$  level structure of  $^{87}Rb$ . The ground state of the cooling transition is the  $|F = 2\rangle$  state within the  $5^2S_{1/2}$  manifold, while the excited state is the  $|F' = 3\rangle$  within  $5^2P_{3/2}$ . These states correspond to the  $|g\rangle$  and  $|e\rangle$  states in the description of the optical molasses in section 2.1. On the other hand, the simplified description of the restoring force is not directly applied as in our case the Zeeman effect splits the ground and excited states to manifolds of 5 and 7 sub-states respectively. Nevertheless, restoring and trapping is indeed present. In the figure we see another transition, called the repump transition. We ought to pump atoms that decay spontaneously to the  $5^2S_{1/2} F = 1$  state, and not the  $5^2S_{1/2} F = 2$ , in order to bring them back into the cooling cycle.

The lasers that were used during the project are:

1. An 80 mW diode laser, denoted DL7140 in figure 5, used for the three counter-propagating laser beams that give rise to cooling, trapping and the extraction of the atomic fountain. The laser is also used for the imaging of the atomic cloud. The diode laser and a corresponding collimating lens were mounted in the beginning of the project.

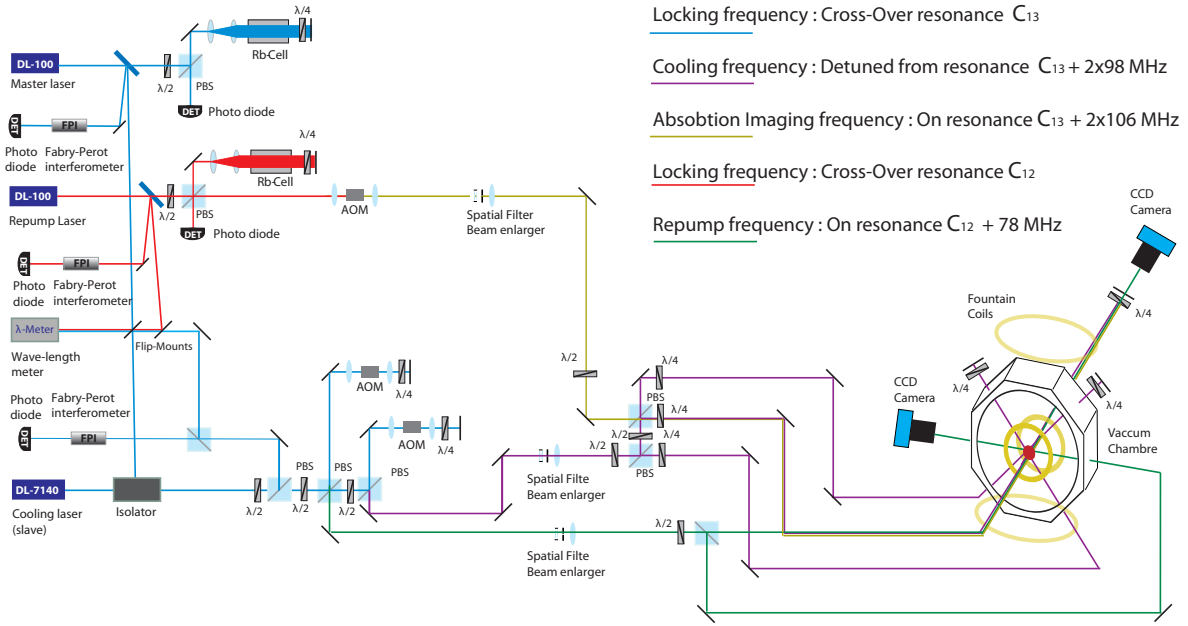


Figure 5: The upper DL100 laser is locked to the cross-over transition  $C_{13}$  using the PDH technique. For that purpose, we use a rubidium vapour cell and a photo diode. A fraction of its intensity is inserted into the main laser, denoted DL7140, through the side of the isolator, introducing injection-locking. The intensity of the DL7140 is divided into three fractions using polarizing beam splitters (PBS) followed by half-wave plates. A fraction goes into a wavelength-meter and a Fabry-Perot interferometer<sup>9</sup>. Another fraction is used for the absorption imaging, and the main fraction for loading the MOT and extracting the fountain. The last two undergo a double-pass through an AOM, which consists on two lenses and a quarter wave-plate, acting as a half wave plate for a retro-reflected beam. Using two PBSs we divide the main fraction of the light field into three orthogonal beams that intersect in the center of the vacuum chamber. The laser fields configuration described in section 2.2, including polarization, is achieved by six quarter-wave plates and three retro-reflecting mirrors. The lower DL100 laser is locked to cross-over transition  $C_{12}$  using the PDH technique as well. It passes through an AOM in order to shift its frequency to resonance with the repump transition.

2. A grating-stabilized<sup>10</sup> diode laser, the upper laser denoted DL100 in the figure, used for stabilizing the main (DL7140) laser. The laser is normally used for a different experiment and we use only a small fraction of its intensity.
3. A second grating-stabilized diode laser, the lower DL100, used for both experiments to drive the repump transition. In the other experiment, this laser is also used for stabilizing an optical cavity as well as for driving the STIRAP transition, corresponding to the schema described in section 1.2.

In order to have a stable MOT, it is substantial to avoid any fluctuations in the wavelengths on which the lasers are lasing. Stability of lasers is maintained by 'locking' them. The second and the third lasers are locked using a combination saturated absorption spectroscopy [14], the Pound-Drever-Hall (PDH) technique [4] and a proportional-integral-derivative (PID) controller, explained in section A. The second is locked to the mid-way between the transitions  $5^2S_{1/2}F = 2 \rightarrow 5^2S_{3/2}F' = 1$  and  $5^2S_{1/2}F = 2 \rightarrow 5^2P_{3/2}F' = 3$ , referred to as a cross-over transition and denoted as  $C_{13}$  in figure 6. The first (slave) laser is then locked

<sup>10</sup>The wavelength of a diode laser within a grating can be pulled by changing the grating's angle slightly. It provides us with a way to shift the wavelength with a very high precision as well as to stabilize it, as explained in section A

to the same frequency by injection-locking, injecting a fraction of the intensity of the second (master) laser into it, as explained in section 3.1.1. We then shift its frequency from the cross-over transition by  $196 \text{ MHz}$ , so that it is red-detuned by  $16 \text{ MHz}$  from resonance with the cooling transition, in order to optimise the trap. Shifting of the frequency is done using an acousto-optical modulator<sup>11</sup>. The beam does a double-passage through the AOM, each time shifted by  $98 \text{ MHz}$ . A fraction of the intensity is shifted in the same manner by  $212 \text{ MHz}$ , so that it is on resonance with the transition. Light on resonance is best absorbed by the atoms, and we use it for absorption-imaging, explained in section 4.2.1. We have set a beam-path for the absorption imaging, including the AOM<sup>12</sup>, a spatial filter for the beam-profile and two cameras, so that we can observe the MOT and the atomic fountain in two orthogonal directions, allowing us to fully characterise its spatial properties. The third laser is locked to the cross-over transition between  $5^2S_{1/2}F = 2 \rightarrow 5^2S_{3/2}F' = 1$  and  $5^2S_{1/2}F = 2 \rightarrow 5^2P_{3/2}F' = 2$ , denoted as  $C_{13}$  in figure 6. We then shift its frequency by  $78 \text{ MHz}$  so that it is on resonance with the repump transition.

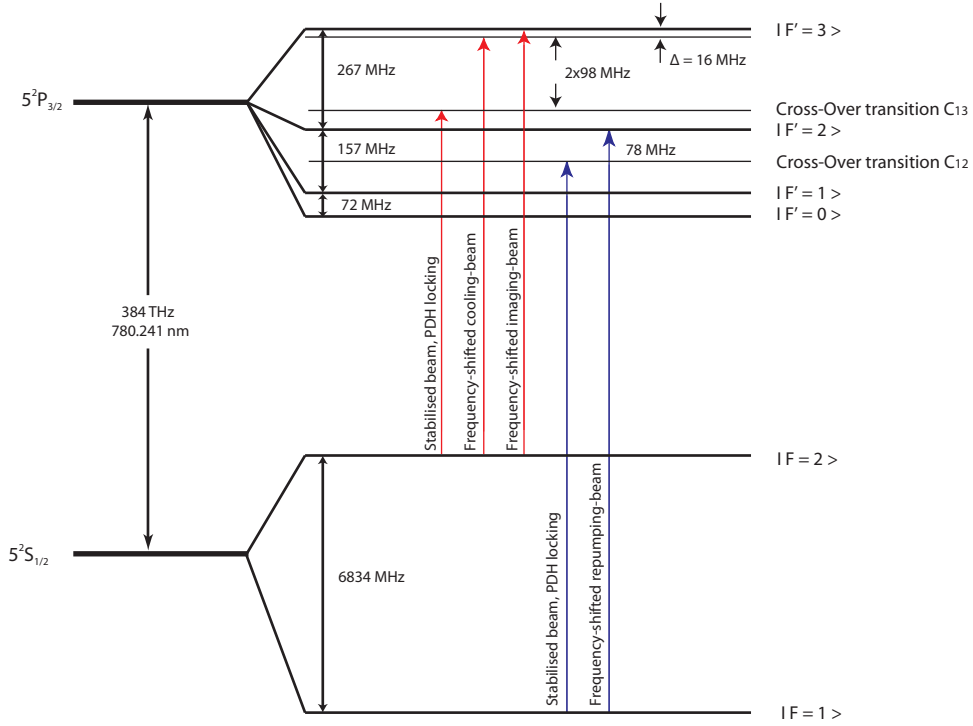


Figure 6: The level structure exploited for the experiment. The transitions between the  $5^2S_{1/2}$  and  $5^2P_{3/2}$  manifolds is called the  $D_2$  line. The left red arrow stands for the cross-over transition  $C_{13}$  into which the cooling laser is locked, as explained in the text. The middle red arrow stands for the frequency-shifted laser beam that is detuned from resonance with the cooling transition, used for the MOT and the atomic fountain. The right red arrow is the frequency-shifted laser beam which is on resonance with cooling transition, used for absorption-imaging. The left blue arrow stands for the cross-over transition  $C_{12}$  into which the repump laser is locked. The right blue arrow stands for the frequency-shifted laser beam that is on resonance with the repump transition in order to drive atoms back into the cooling process.

<sup>11</sup>AOMs are optical instruments that shift the frequency of a light beam by the frequency of the sound wave propagating through them. They allow us to both shift the frequency of the laser and control its intensity.

<sup>12</sup>Setting an AOM consists on its intergration in the beam-path, as well as setting an AOM-driver. The AOM driver consists on voltage-controlled oscillator (VCO), determining the frequency of the sound-waves within the AOM, and a few amplifiers.

### 3.1.1 Injection locking

By injecting a fraction of a (master) laser-beam into a (slave) laser-diode, referred to as a free-running laser, we stimulate emission of photons into the mode of the injected beam which consists both on its frequency and polarization. In other terms, the injected signal is amplified within the medium of the free-running laser-diode. The closer the injected mode is to the free running one, the higher is its amplification. Then, when the difference in frequency of the two lasers is close enough, the injected mode takes over from the free-running mode. Namely, all the intensity is being emitted into the injected mode. The laser is then injection-locked. The minimal detuning of the lasers at which injection locking is possible is given by the relation:

$$|\omega_s - \omega_m| \leq \frac{\omega_s}{Q_e} \sqrt{\frac{I_m}{I_s}} \quad (16)$$

where 'm' and 's' stands for master and laser slave respectively and  $Q_e$  is the energy decay rate of the diode.

Since any light field that enters the laser-diode can cause injection pulling, an optical isolator is placed in front of the diode. Stable injection-locking consists on optimized alignment of the master laser light through the isolator into the free-running laser-diode. Characterization of the new laser-diode's modes-structure is shown in figure 7. In the graph, we see the frequency as a function of the current driving the diode for different temperature. We see that for a constant temperature the frequency increases linearly with the current, and jumps from one mode to the following around critical frequencies. That is representative of the periodicity of the gain profile of the diode, acting as a resonator. We find that never does the free-running laser-diode lase on the desired wavelength that corresponds to the  $C_{13}$  cross-over resonance, as shown in the graph on the right in figure 7. That means that we could not drive it to a frequency obeying equation 16, then lock it by injecting the master laser beam. Nevertheless, we find a major difference in the mode structure when the master beam is injected all along the process, graph on the left in figure 7. The slave laser then has modes around the desired frequency. When it jumps to one of these modes it is still injection-pulled and by varying the current slightly we introduce injection locking. Typically we inject a fraction of 0.8 *mW* and we find a critical frequency detuning of 0.002 *nm*.

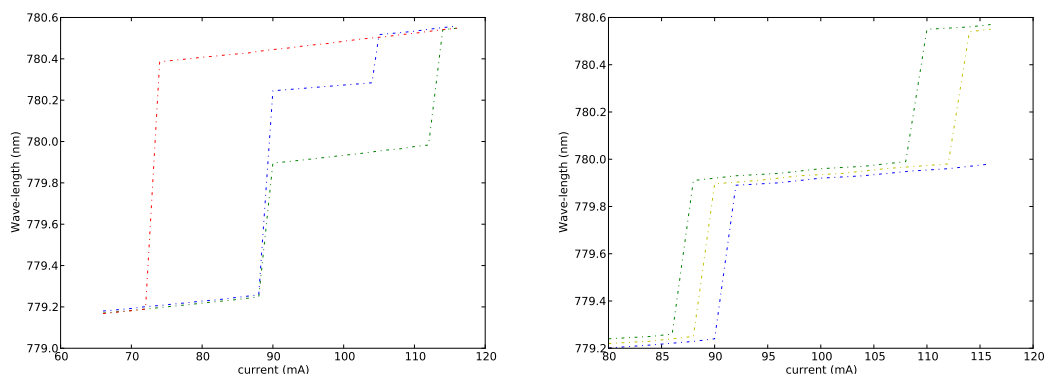


Figure 7: The graph on the right shows the wavelength as a function of the current driving the laser-diode for three different temperatures,  $T = 20.4$ ,  $T = 20$ ,  $T = 19.6$ . from top to bottom. Sharp jumps between modes make it impossible to pull the laser to the required wavelength  $\lambda = 780.2465$ . The graph on the left shows the wavelength as a function of current when increasing it (green), when decreasing it (red) and when the master laser-beam is injected (blue). We encounter a hysteresis-like behavior when the master laser-beam is not injected.

## 3.2 System control

Control of the system is done using a high-performance DAQ board that we have installed for this purpose. Correspondingly, we programmed a LabView code in order to control the experimental set-up and its imaging. Measurements and control are done in two different modes:

1. A continuous control of the trap. Consists on the control of both the frequency and the amplitude of the cooling laser through the AOM and on the control of the magnetic fields through the coils. Switching on and off of the coils is done through a transistor circuits that we made for that purpose. The program enables us the continuous imaging of the vacuum chamber allowing us to align and optimize the MOT.
2. Execution of synchronized waveforms to a number a channels with a resolution up to 1 *MHz*. This program is essential for running an experiment on the time scale of the *ms*. An example of such an experiment, used for the extraction of the atomic fountain, is shown in figure 14. Another main purpose of the program is time-of-flight measurement, explained in section 4.2.2. The program creates a waveform for each of its channels according to the time and amplitude parameters that we choose and passes it to the DAQ board which executes them in parallel. Furthermore, the program enables us to execute a series of sequences, each time changing a different parameter, as well as the executing the same sequence several times and averaging the results.

## 4 The trap

### 4.1 Loading measurements

The beginning of the project overlapped the end of another, whose goal was to prepare a MOT. Therefore, the first goal of the project was to enhance the trap and then characterize it. The steady-state number of atoms confined in the MOT is given by the balance between the loading rate  $R_f$  and the loss coefficient  $\gamma$  [28]:

$$\frac{dN(t)}{dt} = R_f - \gamma N(t) \quad (17)$$

with the solution:

$$N(t) = \frac{R_f}{\gamma} (1 - e^{-\gamma t}) \quad (18)$$

where  $R_f = \frac{n_v V^{2/3} v_c^4}{2 \langle u_v \rangle^2}$ , with  $n_v$  the density of the background vapor,  $\langle u_v \rangle$  the most probable velocity of atoms in the background vapor,  $V$  the trapping volume and  $v_c$  is the critical trapping-velocity. The trapping volume was enlarged by enlarging the laser beam diameter to 12 *mm*, using an objective. We focus the beam into a 20  $\mu\text{m}$  pin-hole, acting as a spatial-filter, using a lens with a focal length of 0.1 *mm* and then we collimate it with a second lens. We set-up the spatial filter in order to avoid the irregular intensity profile of the beam coming out of the diode laser. Furthermore, the new diode laser that we have set-up provides us with higher intensities. Increasing the intensity increases, to a certain extent, the loading rate, as we see in figure 8. The effect of the intensity is through the critical trapping velocity which is determined by the detuning of the laser and the Rabi frequency, and can be deduced from the damping force.

In order to measure the loading rate of the MOT we measure the intensity scattered from it, and detected by a camera, as a function of time. The detected intensity is then divided by the intensity which is expected to be scattered by one atom, which is the expression for

$R_{scatt}$  that is given in equation 8. After optimisation of the apparatus, we find loading rates on the order of  $10^7 s^{-1}$ . A typical number of trapped atoms is on the order of  $10^8$  and loading times on the order of 10 s.

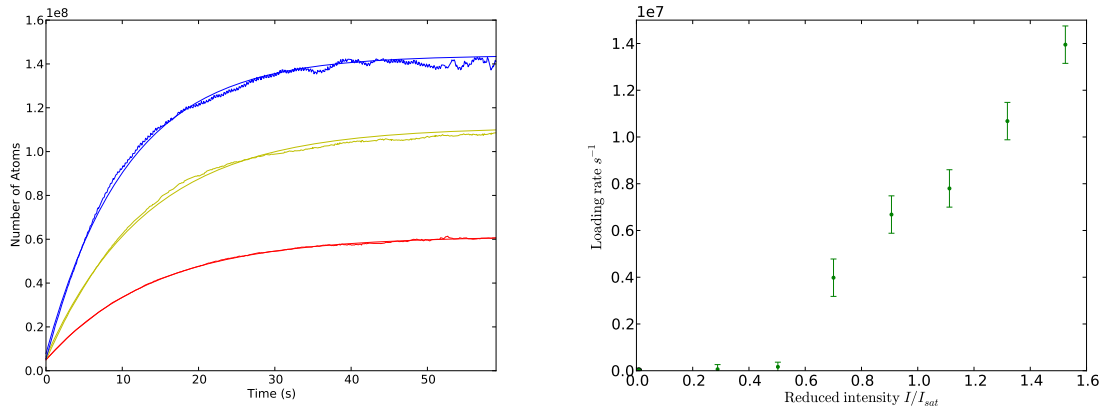


Figure 8: On the left are three loading graphs, and the corresponding theoretical fits, for  $I/I_{sat} = 1.5$ , 1.1, 0.7 in blue, yellow and red respectively. The fits are done according to equation 17. On the right is the dependence of the loading rate upon the intensity. Measurements were taken with a background pressure  $P = 4.2 \cdot 10^{-10}$  mBar and a detuning  $\Delta = -2.5\Gamma$ .

## 4.2 Temperature measurements

### 4.2.1 Optical depth

Observing the MOT directly, namely with continuous imaging, does not allow us to get a hold of processes of the order of a few *ms*. For these time scales we use a different technique. We set-up a probe beam which crosses the atomic cloud and then captured by a camera. With the probe beam set to resonance with the cooling transition, we then get an illuminated image with a shadow. From the absorbed intensity we can then derive the optical depth of the atomic cloud, which is a dimensionless quantity that gives a measure of how opaque a medium is, following its definition:

$$\frac{I}{I_0} = e^{-\tau} \quad (19)$$

where  $I$  is the intensity of the probe beam after the passage through the medium,  $I_0$  the initial intensity of the probe beam and  $\tau = N\sigma_0/A$  the optical depth, with  $\sigma_0$  the atom's cross section. In our case, all variables in equation 19 are space-dependent with the coordinate  $(x, y)$  in the plane perpendicular to the probe's direction of propagation. Hence, the optical depth is the distribution  $\tau(x, y) = \int n(x, y, z)\sigma_0 dz$ . Likewise, if we wish to find the number of atoms in the cloud we perform an integration:

$$N = \frac{1}{\sigma_0} \int dx \int dy \frac{\ln(I_{probe}(x, y) - I_{dark}(x, y))}{\ln(I_{shadow}(x, y) - I_{dark}(x, y))} \quad (20)$$

### 4.2.2 Time-of-flight

Following equation 5 we see that if we know the mean velocity of the atoms in the atomic cloud, we can derive its temperature. In order to measure the mean velocity, we use a technique called time-of-flight (TOF). The atoms, initially trapped in the MOT, are released

by turning off the cooling beams so that the atomic cloud expands, and we assume with the atoms' mean velocity:

$$r^2 = r_0^2 + \left(\frac{k_B T}{m}\right)^2 \cdot t^2 \quad (21)$$

We load and release the MOT several times, and measure its optical depth distribution at different delays from the time of release. For every delay we take a few measurements and fit a 2D Gaussian distribution to their average, using Matlab. Subsequently, we fit the full widths at half maximum of the distributions to equation 21. The temperature is then deduced from the slope of the fit's asymptote. An example is shown in figure 9, where we measured  $\langle v_x \rangle = 0.0786$  and  $\langle v_y \rangle = 0.0764$ , that corresponds to  $T_x = 64.6 \mu K$  and  $T_y = 61 \mu K$ .

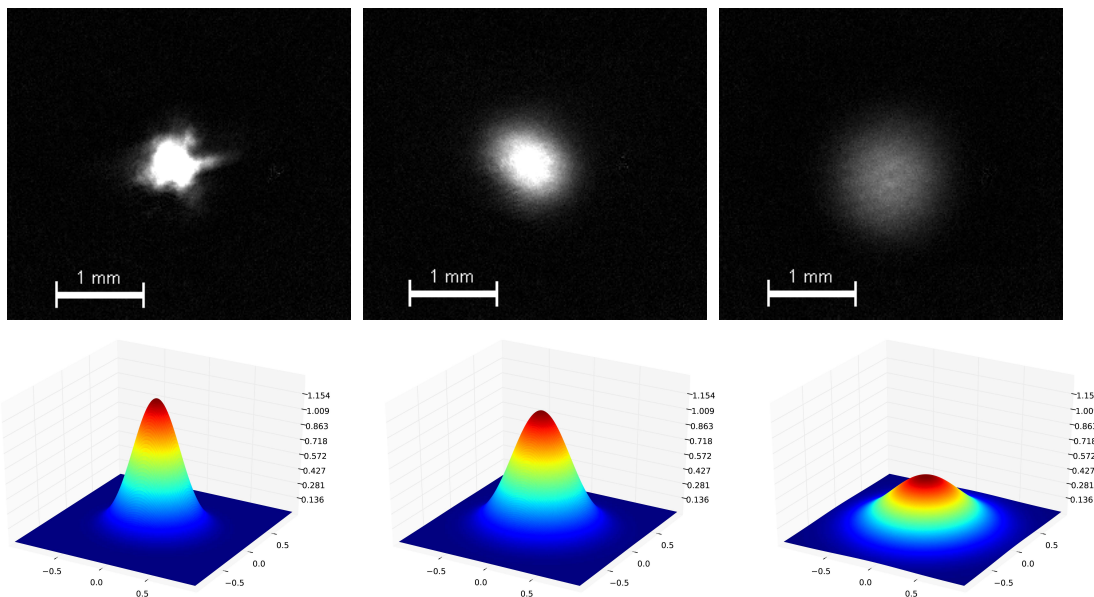


Figure 9: Three out of a series of images used for a temperature measurement. Above are the optical depths of the atomic cloud at in times 0, 2 and 4 *ms* from the time of release. Below are the corresponding Gaussian fits used for the calculation. The fits are made using Matlab.

Although the polarizations of counter-propagating laser fields in the MOT are circular and opposite, the steady-state temperature of the atomic cloud is generally expected to be on the order of the Doppler limit. It is the magnetic field that induces inhibition of the polarization gradient processes. Nevertheless, it was shown [19, 36, 39] that for sufficiently low, intensities temperatures well below the Doppler limit can indeed be achieved. Since it is of high importance that the atomic cloud is as cold as possible, we examine its further cooling. Leaving the laser fields after having turned off the magnetic field of the MOT we induce further sub-Doppler cooling. The models for 1D polarization gradient cooling are not easily extended to a 3D description. In a 1D configuration, the final temperature due to polarization gradient cooling scales with the light shift of the ground states<sup>13</sup> [26]:

$$k_B T_{lim} = b \Delta E_g \quad (22)$$

where the coefficient  $b$  depends upon the polarization configuration, and is 0.097 for the  $\sigma^+$  -  $\sigma^-$ . The light shift  $\Delta E_g$  is given by:

<sup>13</sup>The light shift is the difference in energy between the eigenvalue of the unperturbed Hamiltonian, and the perturbed Hamiltonian, in the presence of the radiation.

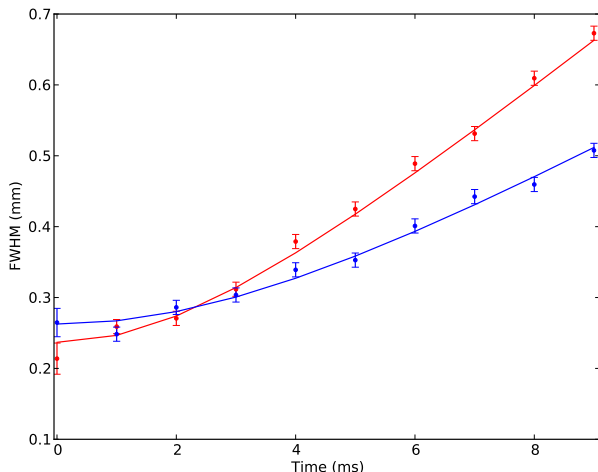


Figure 10: The full width at half maximum of the atomic cloud distribution as a function of time after it was released from the trap. In red is the evolution of the atomic cloud as it spreads after both the magnetic field and the cooling beams were turned off. In blue is the evolution of the atomic cloud starting 10 *ms* after the trap was released but the cooling beams were still on, inducing further molasses cooling. For the first we find 61  $\mu K$  and for the second 25.1  $\mu K$ . The theoretical fits are deduced by equation 21.

$$\Delta E_g = \frac{I}{I_{sat}} \cdot \frac{\hbar \Delta C_{ge}^2}{1 + (2\Delta/\Gamma)^2} \quad (23)$$

with  $C_{ge}$  being the Clebsch-Gordan coefficient of the considered transition, typically on the order of 0.1.

Hence, in the limits  $\Delta \gg \Gamma$  and  $\Omega \ll \Delta$ , we expect  $k_B T = \hbar C_{ge}^2 \cdot \Omega^2 / |\Delta|$ ; the final temperature is linearly increasing with the intensity and linearly decreasing with the magnitude of the detuning<sup>14</sup>. Our observations, shown in figure 11 coincide with these expectations. We find a gain of 65  $\mu K / |\Delta|^{-1}$  for detunings obeying  $\Gamma / |\Delta| \leq 1$ , and of 30  $\mu K / I$  for intensities obeying  $I / I_{sat} \approx 1$ . We achieve temperatures in the sub-Doppler regime, on the order of 10  $\mu K$ .

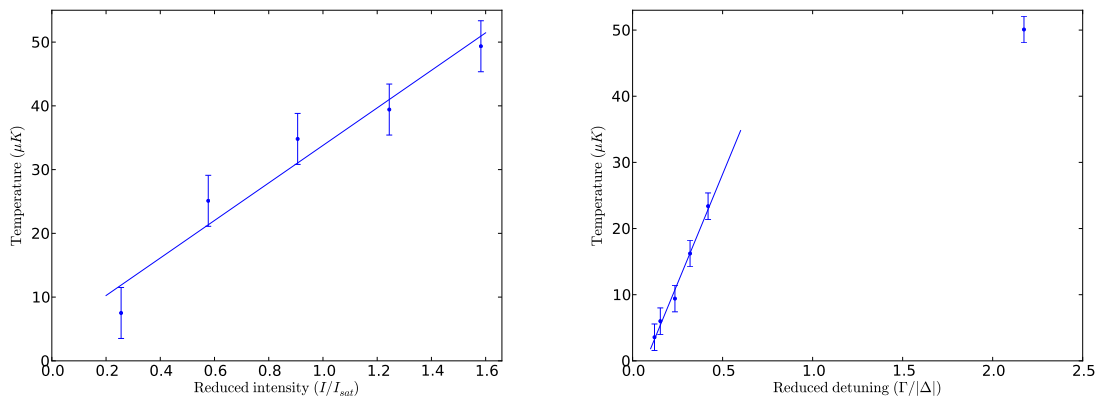


Figure 11: On the left is the temperature of the atomic cloud as a function of the reduced laser fields intensity  $I/I_{sat}$ , for  $|\Delta|/\Gamma = 2$ . On the right is the temperature of the atomic cloud as a function of the reduced parameter  $|\Delta|/\Gamma$ , for  $I/I_{sat} = 1.5$ . The temperatures were measured after 10 *ms* of interaction with the laser fields in the absence of a magnetic field, inducing polarization-gradient cooling.

<sup>14</sup>Note that the atomic cloud cannot be cooled to arbitrarily low kinetic temperatures, as the model will no longer be valid when the recoil velocity is close to the width of the velocity distribution. The coldest kinetic temperature ever measured utilising a 3D molasses cooling of Cs is  $2.5 + 0.6 \mu K$  [32]

## 5 Atomic fountain

### 5.1 Moving molasses

Once the MOT was optimized and low temperatures in the sub-Doppler regime achieved, the main goal was to setup the fountain for extracting atoms from it. The classical way of doing so, utilized as well by researchers from Dr. Kuhn's group, is to use different detunings for the beams propagating upwards and those propagating downwards which creates an imbalance of the radiation pressure along the vertical, following equation 8. Nevertheless, during this project we had created an atomic fountain in a different way which rely on the effective detunings of the lasers due to the Zeeman splitting of the atomic levels in the presence of a uniform magnetic field, as demonstrated in figure 12. The different effective detunings of two counter-propagating laser fields induces a cooling process in a moving frame, namely, producing a moving molasses. In the figure, the dashed lines stand for the laser frequency, taking into account the Doppler shift. For  $v = 0$ , the frequency of both the lasers are equal, but as they are coupled to different transitions, following the conservation of angular-momentum, their detunings are different. The detuning of the laser propagating downwards is farther from resonance with the transition to which it is coupled than the laser field propagating upwards to its corresponding transition. Hence, there is a radiative force pushing the atoms upwards. It is only for a resonant velocity  $v = v_r$ , that the two laser fields frequencies, incorporating as well the Doppler shift, are equally detuned from resonance with their corresponding transitions. This gives rise to cooling to finite velocities.

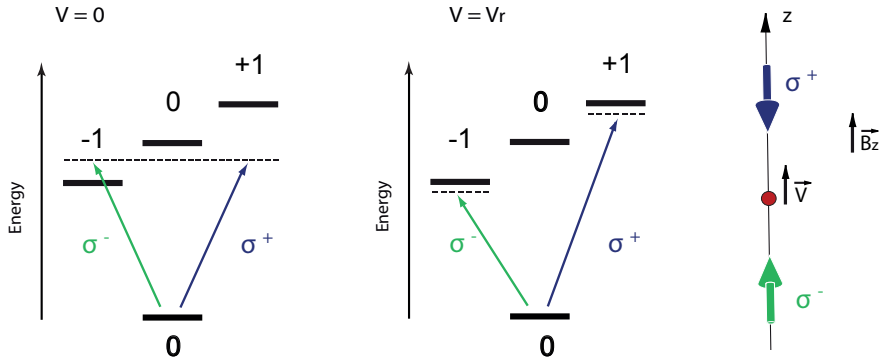


Figure 12: The simple case of  $|F = 0\rangle$  and  $|F = 1\rangle$  level structure in the presence of a uniform magnetic field. The dashed lines stand for the laser frequency, taking into account the Doppler shift. In the case of a static atom, the  $\sigma^-$  laser is more strongly coupled to its corresponding transition and the atom is being pushed upwards. For an atom moving at the resonant velocity  $v_r$ , both lasers are equally detuned from their corresponding transition. The atom's velocity is hence damped in a frame moving at the resonant velocity.

Most simply,  $\mathbf{F} = \mathbf{F}(\delta_1) + \mathbf{F}(\delta_2) = 0$  when  $\delta_1 = \delta_2$ . A more general form of equation 13, for the detuning of a laser field with polarization  $s \in \sigma^-, \pi, \sigma^+$  from a dipole transition of two states that are separated by  $\Delta M_J \in -1, 0, 1$  respectively, can be written as follows:

$$\delta(\mathbf{v}) = \omega_l - (\omega_0 + \omega_L \cdot \Delta M_J + \mathbf{k} \cdot \mathbf{v}) \quad (24)$$

Thus, counter-propagating laser beams, coupled to two dipole transitions with angular-momentum separation  $\Delta M_{J,1}$  and  $\Delta M_{J,2}$ , are equally detuned from resonance with their respective transitions in a frame moving at the resonant velocity:

$$v = n \frac{g_J \mu_B}{2\hbar k} \cdot B \quad (25)$$

with  $n = \Delta M_{J,2} - \Delta M_{J,1} \in -2, -1, 0, 1, 2$ .

Each value of  $n$  corresponds to the difference in angular-momentum between the two ground-state sub-levels of the two driven transitions. Furthermore, each value correspond to a possible coherent two-photon velocity-selective resonance (VSR) between ground-state sub-levels separated by angular momentum  $n$  [34], shown in figure 13, which is the underlying factor of cooling to finite velocities. Namely, the cooling process is attributed to a momentum transfer between the two counter-propagating laser fields by a coherent two-photon transition between two ground-state sub-levels. The transition occurs only when the atom is moving at the resonant velocity, given by equation 25.

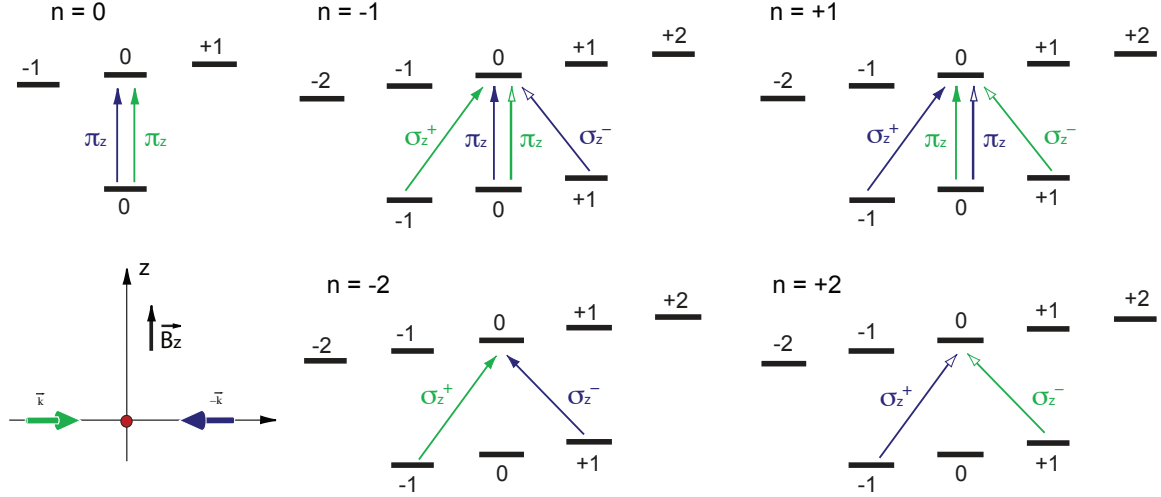


Figure 13: The seven possible coherent two-photon transitions between ground-state sub-levels, represented by pairs of solid arrows or open arrows. Each value of  $n$  corresponds to the difference in spin of the photons giving rise to the transition. The  $^{87}\text{Rb}$  level scheme that we exploited in the experiment, shown in figure 6, splits to a five ground-states to seven excited-states level-structure. We denote the polarization with the label  $z$  as we are interested in its projection on the quantization axis, where the Zeeman split is defined.

## 5.2 3D configuration

The extraction of the fountain is divided into three steps, as shown in figure 14.

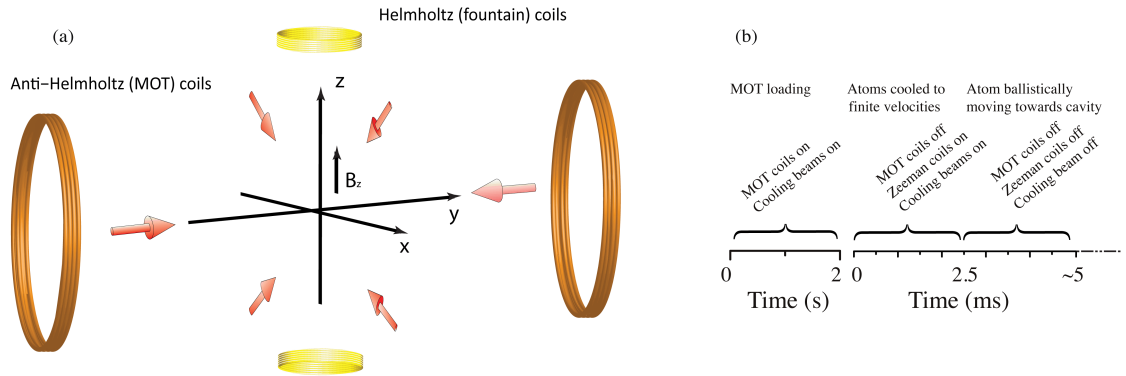


Figure 14: (a) The experimental setup. The MOT coils' axis is aligned along  $y$ , while the fountain coils' axis along  $z$ . One pair of counter-propagating laser fields is parallel to  $y$ , while the other two are located in the  $x - z$  plane, aligned in  $45^\circ$  with respect to  $z$ . (b) The launching process.

The first step is the loading of the atomic cloud, as described in section 4.1. Once the atomic cloud is loaded, we release it by turning off the trap's magnetic field, keeping the laser fields present. Simultaneously we turn on a uniform magnetic field, pointing upwards, induced by the Helmholtz coils. In the presence of the magnetic field and the laser fields, the moving molasses scheme is applicable for each pair of counter-propagating laser fields. Each pair cool the atoms to a velocities obeying equation 25 along its axis. Cooling to all five velocity groups is indeed observed. The magnitude of the velocity within each velocity-group is governed by the amplitude of the magnetic field while the selection of the velocity groups is essentially due to the projection of the polarization vector of the laser beams on the quantization axis, defined by the direction of the magnetic field. It is the composition of multiple velocities along different axes that gives rise to the extraction of more than one atomic fountain from the MOT.

The quantization axis is effectively the axis along which an atom measures a photon's polarization. Hence, a photon propagating along the  $z$  axis can drive only dipole transition with separation  $\Delta M_J = \pm 1$ , which correspond to the two possible eigenvalues for its polarization states along its axis of propagation<sup>15</sup>. Nevertheless, in our setup, none of the laser fields is parallel to the magnetic field<sup>16</sup>, as shown in figure 14. As a result, each of the beams is coupled to all of the dipole transition, but with different amplitudes, due to the projection of their polarization on the quantization axis.

We consider a light field of general polarization propagating along an axis  $z'$  that creates an angle  $\theta$  with  $z$ :

$$E(z, t) = \tilde{E}_0(A'\hat{\epsilon}^{\dagger'} + B'\hat{\epsilon}^{\hat{-}'})e^{ikz'}e^{-i\omega t} + c.c \quad (26)$$

where  $\hat{\epsilon}' = A\hat{\epsilon}^{\dagger'} + B\hat{\epsilon}^{\hat{-}'}$  is the normalized polarization vector with :

$$\begin{aligned} \hat{\epsilon}^{\dagger'} &= \frac{\hat{\epsilon}_{x'} + i\hat{\epsilon}_{y'}}{\sqrt{2}} \\ \hat{\epsilon}^{\hat{-}'} &= \frac{\hat{\epsilon}_{x'} - i\hat{\epsilon}_{y'}}{\sqrt{2}} \end{aligned} \quad (27)$$

Transforming the field to the quantization frame  $z$  we get  $\hat{\epsilon} = A\hat{\epsilon}^{\dagger} + B\hat{\epsilon}^{\hat{-}} + C\hat{\epsilon}_z$  with<sup>17</sup>:

$$\begin{aligned} A &= \left[ A' \cos^2 \frac{\theta}{2} - B' \sin^2 \frac{\theta}{2} \right] \\ B &= \left[ -A' \sin^2 \frac{\theta}{2} + B' \cos^2 \frac{\theta}{2} \right] \\ C &= -i(A + B) \sin \theta / \sqrt{2} \end{aligned} \quad (28)$$

We regard these amplitudes as probabilities, the diagonal elements of a photon's polarization density matrix in the basis of  $z$ . Hence,  $|A|^2$ ,  $|B|^2$  and  $|C|^2$  are the amplitudes of the expectation values of the angular-momentum of a photon along  $z$  and also the relative probabilities to be coupled to a  $\Delta M_J = +1$ ,  $\Delta M_J = -1$ ,  $\Delta M_J = 0$  dipole transition, respectively. The amplitudes for each of the beams is given in table 5.2.

From these amplitudes, we can get an idea of which coherent two-photon resonance is most likely to occur along each of the axes and hence which velocity group is most likely to be observed. Along the  $y$  axis, we find that the most probable resonance is between two

<sup>15</sup>Although photons are spin-1 particles, as they are massless particles, the eigenvalue  $M_J = 0$  is prohibited and their two spin states are referred to as polarization states.

<sup>16</sup>Since the magnetic field must point towards the cavity, no beam can coincide with that direction because they will 'clip' on it.

<sup>17</sup>These amplitudes can be achieved using a quantum-mechanical formulation as well.

$\mathbf{k}/ \mathbf{k} $	Polarization	$p(\sigma_z^+)$	$p(\sigma_z^-)$	$p(\pi_z)$
$(0, 1, 0)$	$\sigma_k^+$	0.25	0.25	0.5
$(0, -1, 0)$	$\sigma_k^-$	0.25	0.25	0.5
$(1, 0, 1)/\sqrt{2}$	$\sigma_k^-$	0.02	0.73	0.25
$(-1, 0, -1)/\sqrt{2}$	$\sigma_k^+$	0.73	0.02	0.25
$(-1, 0, 1)/\sqrt{2}$	$\sigma_k^-$	0.02	0.73	0.25
$(1, 0, -1)/\sqrt{2}$	$\sigma_k^+$	0.73	0.02	0.25

axis	$p(\Delta M_J = -2)$	$p(\Delta M_J = -1)$	$p(\Delta M_J = 0)$	$p(\Delta M_J = +1)$	$p(\Delta M_J = +2)$
$y$	0.06	0.25	0.38	0.25	0.06
$x = z$	0.00	0.01	0.09	0.37	0.53
$x = -z$	0.00	0.01	0.09	0.37	0.53

Table 1: Upper table: each row corresponds to one of the six laser fields in the setup. We refer to the laser fields through their direction of propagation  $\mathbf{k}/|\mathbf{k}|$  with respect to the notations in figure 14. The polarization column refers to the polarization along the axis of propagation. The columns  $p(\sigma_z^+)$ ,  $p(\sigma_z^-)$ ,  $p(\pi_z)$  stand for the amplitudes of the projection of the polarization along the quantization axis  $z$ . Lower table: the deduced probability  $p(\Delta M_J)$  of having the two laser fields coupled to two different ground-state sub-levels with an angular-momentum difference  $\Delta M_J$ . Each row corresponds to one of the three axes along which there is a pair of counter-propagating laser field.

ground-state sub-levels with an angular-momentum separation of  $n = 0$ , since the  $\pi$  element of the projection of the polarization of the laser fields is most important. Along the  $z = \pm x$ , the most probable resonance corresponds to an angular-momentum separation of  $n = +2$ . Furthermore, we see that the  $n = -2, -1$  are not likely to be observed, all with  $p \leq 0.01$ .

These values can be used only to a certain extent. Most simply, because the coupling do not depend solely upon the photon's polarizations amplitudes, but also on the atom's ability to undergo the transition with the corresponding angular-momentum separation. The implication of these amplitudes has a considerable validity in a steady state solution. Nevertheless, one must consider the temporal evolution of the atom's density matrix. For example, if an atom with a three ground-states to five excited-states level-structure is pumped into the  $|F = 1, m_F = 0\rangle$  ground-state, no two-photon transition within the  $n = +2$  group can occur, even if it is favored by the polarization of the light field. Furthermore, one must consider the unequal spontaneous decay into the different sub-levels in the ground-state manifold.

The velocity-selective resonance can naturally be represented in the dependence of the force upon velocity. We expect a line shape similar to the force shown in figure 3, only crossing  $\mathbf{F} = 0$  not only at  $\mathbf{v} = 0$  but for the other resonant velocities as well. As the atom never achieves a steady state in these circumstances, see section 2.3, in order to derive the force exerted on the atom, one must first derive its time-dependant expression and proceed by averaging over a time that corresponds to the movement of an atom along a wavelength. Attempts to do so were undertaken using Matlab, based on reference [37]. The procedure is described appendix D, but as the goal of the project was to mount the fountain for it to be used for the insertion of single atoms into optical cavities, efforts were put into the experimental demonstration of the fountain rather than a numerical or analytical ones. Nevertheless, our observations are in agreement with the values given in table 1.

## 5.3 Observations

### 5.3.1 Three atomic fountains

In figure 15 we show the observation of the atomic fountains extracted from the MOT. The three atomic fountains are cooled to the resonant velocity  $v = 1.74 \frac{m}{s}$  along the vertical  $z$ , and to the resonant velocities  $v = -1.36, 0, +1.36$  along the horizontal  $y$ .

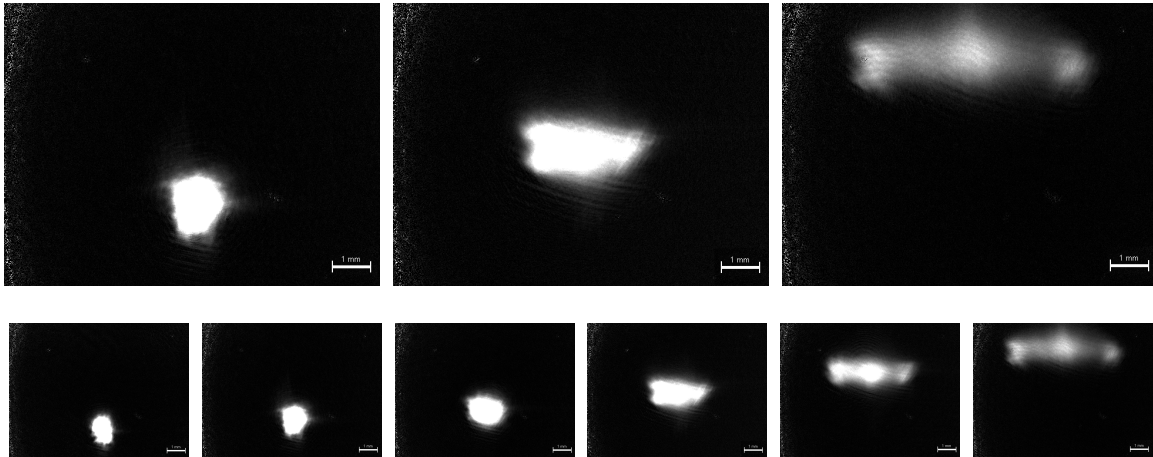


Figure 15: Three atomic fountains extracted from the MOT. It is a view on the  $z - y$  plane, with respect to the axes in figure 14. The time delay between two sequential images is  $1 \text{ ms}$  and  $0.5 \text{ ms}$ , in the upper series and the lower series respectively. The three moving atomic clouds advance  $4.3 \text{ mm}$  along the  $z$  axis. The outer atomic beams advance  $2.6 \text{ mm}$  along the  $y$  axis. The fountains were extracted using a magnetic field of  $B = 14G$ .

The horizontal velocity is due to cooling of the counter-propagating laser-fields situated along  $y$ , while the vertical velocity is due to the cooling of the counter-propagating laser fields within the  $z - x$  plane. Along each of the two axes  $z = \pm x$ , the atoms are cooled to the resonant velocities following equation 25. The composition of the two velocities along  $x$  cancel-out, as we observe no splitting of the atomic fountain along that axis, and the composition along  $z$  results in the effective resonant velocities:

$$v_z = n \frac{gJ\mu_B}{\sqrt{2}\hbar k} \cdot B \quad (29)$$

Figure 16 shows the measured velocities, on the left, and the measured vertical kinetic temperatures, on the right, as a function of the magnetic field. In green is the measured vertical velocity of the middle atomic fountain, corresponding to the  $n = 0$  velocity-group along  $y$ . The curve shows cooling to the two different velocity groups  $n = +1, +2$ , and no cooling to the resonant velocity-groups  $n = -2, -1, 0$ . This observation coincides with the expectations arising from table 5.2. For the  $n = 2$  velocity-group, observed between  $B = 0.5G$  and  $B = 7G$ , we find a gain of  $0.12 \frac{m}{s}/G$ , while for the  $n = 1$  velocity group, observed between  $B = 8G$  and  $B = 14G$ , we find a gain of  $0.047 \frac{m}{s}/G$ . In blue is the horizontal velocity of the two outer fountains. The large error estimation is due to the spatial overlapping of the three atomic fountains, seen in figure 15. We distinguish the cooling to the  $n = 1$  velocity-group, in the range between  $B = 0.5G$  and  $B = 4G$ , and to the  $n = 2$  velocity-group in the range  $B = 8G$  and  $B = 14G$ . We find gains of  $0.082 \frac{m}{s}/G$  and  $0.049 \frac{m}{s}/G$  respectively. The factor of the gains for the two different velocity-groups along  $z = \pm x$  is found to be 2.55, to be compared with the expected value 2. We attribute this disagreement to the errors, introduced by the limitations of the CCD cameras in use. Note that we did not estimate this factor for the velocity-groups along  $y$  since the overlapping of the extracted fountains prevented us of

taking precise measurements. We measure this factor in a different way, described in section 5.3.2.

On the right we show the vertical temperature of the middle atomic fountain, measured along the  $z$  axis, as a function of the magnetic field. We see that temperatures in the sub-Doppler regime, around  $50 \mu K$ , are achieved for higher values of magnetic field. It is noticeable that for lower magnetic fields, higher temperatures are observed. This observation can be explained by the dispersion-shaped resonant enhancement of the velocity-dependent force exerted on a moving atom [1, 30]. Its width depends upon the damping rate of the coherence, namely, on the rate of excitation followed by spontaneous emission, in contrast to the desired two-photon coherent transitions shown in figure 13. For the damping to be enhanced around the non-zero VSR's, we must require  $\gamma_p \ll \omega_L$  [37], where  $\gamma_p$  is the pumping rate, which depends upon the lasers' intensity and the detuning. It is hence very likely that the temperature can be optimised for the lower magnetic fields by using lower intensities, and higher detunings. Because of lack in time, this feature was not explored during the project. Nonetheless, most of the measurements show temperatures around the Doppler limit.

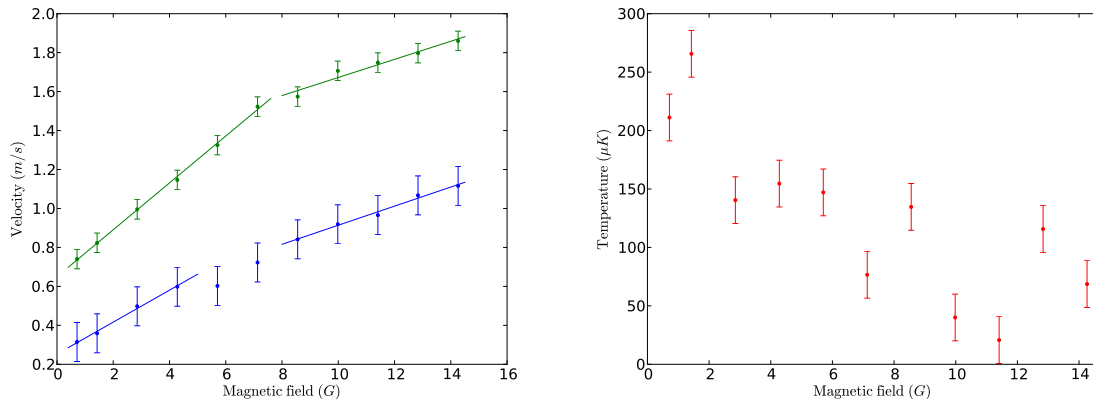


Figure 16: On the left is the vertical velocity of the middle atomic fountain, in blue, and the horizontal velocity of the two outer atomic fountains, in green, as a function of magnetic field. The significant error estimation for the horizontal velocity is due to the spatial overlapping of the extracted atomic fountains. We attribute the offset to the magnetization of the view-ports of the vacuum chamber, together with earth's magnetic field. On the right is the vertical kinetic temperature of the middle atomic beam as a function of the magnetic field.

### 5.3.2 Single atomic fountain

The spatial overlapping of the extracted atomic fountains had caused a significant error estimation in the measurements of the horizontal velocity. We find that a slight imbalance of intensity of the two counter-propagating laser fields along  $y$  favors the  $n = -2, -1$  resonant velocity-groups over the  $n = 0, +1, +2$  velocity-groups. Figure 17 shows an example of the extraction of a single atomic fountain. In this case, atoms are cooled to the resonant velocity-group  $n = -1$  along the horizontal and  $n = +1$  along the vertical. The imbalance is achieved by a very slight misalignment of the laser fields from overlapping one another. We attribute this observation to the slight radiation pressure imbalance that is induced. Note that when no magnetic field is applied after releasing the MOT, keeping the laser fields on, we do not observe a draft in the atomic cloud's position. This means that the measured velocities are induced only by the moving molasses process.

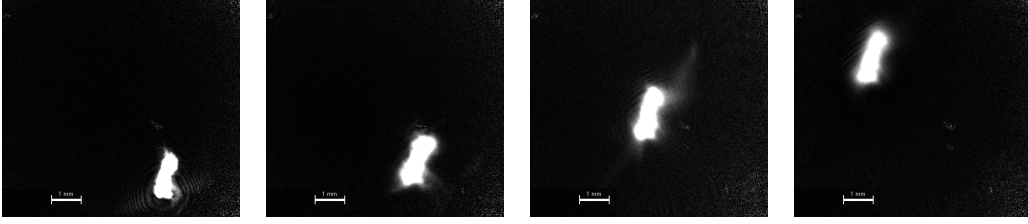


Figure 17: A single atomic fountain, extracted with a magnetic field  $B = 14G$ . Along the vertical the atoms are cooled to the resonant velocity  $2.6 \frac{m}{s}$ , within the  $n = +2$  velocity-group. Along the horizontal the atoms are cooled to the resonant velocity  $1.87 \frac{m}{s}$ , within the  $n = -2$  velocity-group.

Figure 18 shows the measured horizontal velocity, in blue, and the measured vertical velocity, in red. Along both axes, we observe cooling to the  $n = 2$  velocity-group in the range between  $B = 1G$  and  $B = 7.5G$ , and the  $n = 1$  velocity-group between  $B = 8G$  to  $B = 14G$ . Along the vertical, the curves show gains of  $0.207 \frac{m}{s}/G$  and  $0.099 \frac{m}{s}/G$  respectively. Along the horizontal, the curves show gains of  $0.14 \frac{m}{s}/G$  and  $0.0563 \frac{m}{s}/G$ . The factor of the gains of the two different velocity-groups along  $z = \pm x$  and along  $y$  are found to be 2.09 and 2.49 respectively, to be compared with 2. Furthermore, the factor of gains of the  $n = +1$  velocity-group along  $y$  and the same velocity-group along  $z = \pm x$  is found to be 1.48, to be compared with  $\sqrt{2} = 1.41$ . As for the  $n = +2$  velocity-groups along the different axes, we find a factor of 1.76.

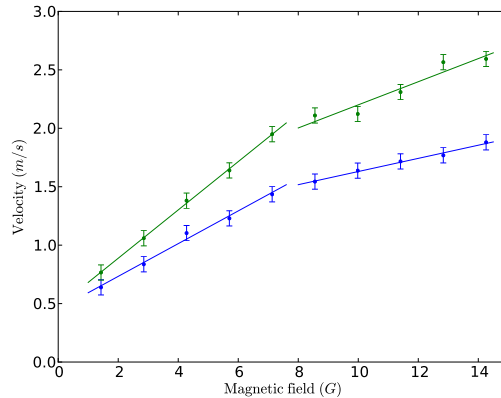


Figure 18: The measured velocities along the horizontal, in yellow, and along the vertical, in red, for the extraction of a single fountain. The atoms are cooled to the same resonant velocity along by all three counter-propagating laser fields, as explained in the text. We attribute the offset to the magnetization of the view-ports of the vaccum chamber, together with earth's magnetic field.

### 5.3.3 Interaction time

In figure 19 we show the final velocities and temperatures to which the atoms are cooled as a function of the interaction time, namely, the time during which the laser fields and the magnetic field are present. These observations are significant for the understanding of the processes as well as because the interaction time in the used set-up is limited. The limitation of the interaction time is due to the limited beam diameter that can be used in the presence of the optical cavity, which is situated above the MOT. On the left, in blue, are the resonant velocities along the  $y$  axis and in green are the resonant velocities along each of the axes  $z = x$  and  $z = -x$ , following  $v_{x=\pm z} = v_z/\sqrt{2}$ . The images are taken in the particular case where

all the atoms are driven to the  $n = -2$  resonant velocity-group along  $y$  and to the  $n = +1$  velocity-group along  $x = \pm z$ , as described in section 5.3.2. On the right are the measured horizontal temperatures.

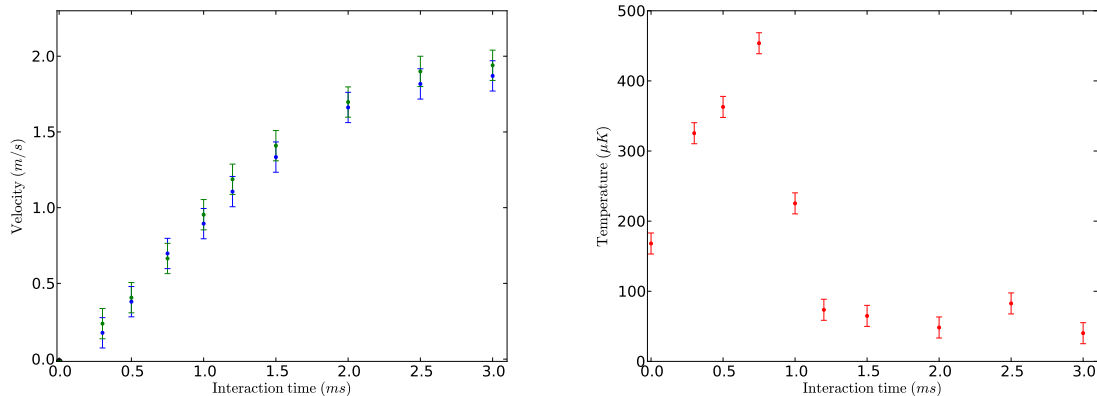


Figure 19: On the left are the final velocities to which the atoms are cooled as a function of the interaction time. In blue are the resonant velocities along the  $y$  axis and in green are the resonant velocities along  $x = \pm z$ , which is a factor of  $2^{-1/2}$  of the observed vertical velocity, as explained in the text. We clearly see that the atoms are being cooled to the same velocity group along both axes. On the right is the horizontal temperature as a function of the cooling time. Measurement are done with a magnetic field  $B = 14G$

During the first  $1.5\text{ ms}$  we find an acceleration of  $0.9885\frac{m}{s}$  along  $y$  and  $0.9884\frac{m}{s}$  along  $z = \pm z$ . The acceleration due to the cooling process is as well shown in figure 21, where we track the explicit motion of the extracted atomic cloud. Furthermore, we observe an important change in the final temperature of the extracted atomic cloud as a function of the interaction time. We find that the cooling time is on the scale of the acceleration time,  $1.2\text{ ms}$  compared to  $2\text{ ms}$ . Nevertheless, we believe that the duration of the passage from the temperature of the MOT, typically in the Doppler regime, to the temperature of a moving molasses, typically in the sub-Doppler regime, can be optimised. The observed duration is partly explained by the heating that is observed in the beginning of the process, which coincides with the measured switching time of the Helmholtz coils, found to be  $55\ \mu s$ . The velocity distribution of the atoms when the trap is released is centered around  $v = 0$ . The damping force around the resonant velocities, obeying equation 25 with  $n = \pm 1$ , occurs instantaneously on the time scale of sub-Doppler laser cooling, which is on the order of a few  $ms$ . In other terms, we are cooling the atoms to velocities one order of magnitude higher than their initial ones. Thus, the atoms' velocity is adiabatically following the passage of the damping force from the  $n = 0$  to the  $n = \pm 1$  velocity group. Exploring a slowly increasing magnetic field might optimise the cooling time of the atomic beams.

In figure 20 we show atomic fountains extracted with an interaction time of  $1\text{ ms}$ , lower series, and  $2.5\text{ ms}$ , upper series. The time separation of two sequential images is  $1\text{ ms}$ , and we clearly see the significant difference in the dispersion of the atomic clouds, representing a the difference in temperature. Furthermore, for lower magnetic fields, we observe the dependence of the cooling processes along orthogonal axes. In the case of figure 20, atoms are cooled to the same resonant velocity-group  $n = +1$  along  $z$ , but to three different velocity-group  $n = -1, 0, +1$  along the horizontal. Nevertheless, it is along  $z$  that we observe a difference in their motion; the outer fountains reach a different height than the middle one. As discussed in section 5.2, the cooling process along each axis is due to coherent two-photon transitions which redistribute the population among the ground-state sub-levels. Consequently, the

redistribution of the population due to the cooling process along one axis naturally restricts its ability to be redistributed for the cooling to occur along a second axis. Most simply, since the cooling processes along different axes are coupled to the same dipole transitions, they are expected to be dependent. This observation is of high importance for the fountain to be utilised for the simultaneous insertion of three single-atoms into three optical cavities. Nonetheless, we did not have time to characterise this feature in the frame of this project.

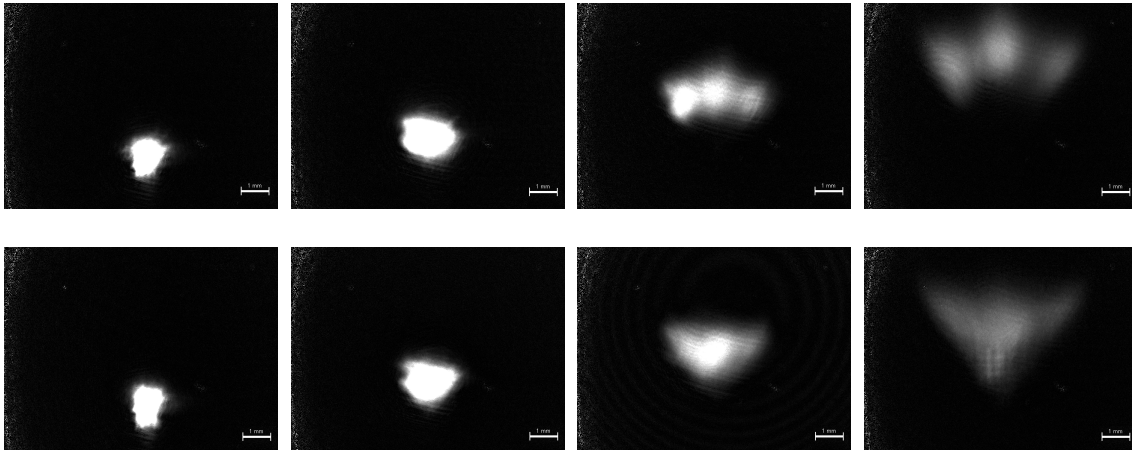


Figure 20: Three atomic fountains extracted from the MOT. It is a view on the  $z - y$  plane, with respect to the axes in figure 14 and each figure is taken 1  $ms$  later than the previous one. The first series shows the case where the interaction time is 2.5  $ms$  and the second where it is 1  $ms$ . We observe significant dependence of the temperature upon the interaction time. In the first series we also observe a different height of the  $n = \pm 1$  resonant velocity-group and the  $n = 0$ .

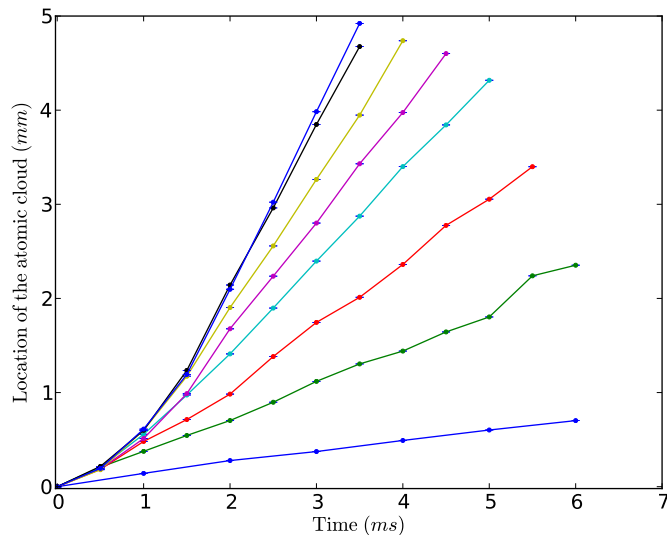


Figure 21: The location of the atomic fountain as a function of time for interaction times 0.3, 0.5, 0.75, 1, 1.2, 1.5, 2 and 2.5  $ms$ . The final velocity converges to  $1.87 \frac{m}{s}$ .

## 6 Achievements

1. We setup a new laser diode and a corresponding collimating lens.  
We characterize its modes structure and the injection-locking for it to be used to run the magneto-optical trap and the atomic fountain.
2. We setup a DAQ-board and program a corresponding Labview code for the precise control of the magneto-optical trap and the atomic fountain.
3. We setup beam paths and cameras for the execution of time-of-flight measurements and for the characterization of the atomic fountain's motion.  
We program a Labview and Matlab codes for the analysis of the absorption imaging for the mentioned puposes.
4. We enhance the MOT and optimise it, setting up the new laser-diode, spatial filters and beam enlargers.  
Finally, we characterise it; we observe temperatures on the order of  $60 \mu K$  for the magneto-optical trap, and on the order of  $10 \mu K$  with further polarization-gradient cooling.
5. We mount the requiered for the extraction of an atomic fountain; We make a pair of Helmholtz coils and transistor circuits.  
We demonstrate a three-directional and a single cold atomic fountains extracted from the magneto-optical trap, using a pair of Helmholtz coils solely. We observe all five possible velocity-groups.  
We characterize the dependence of the velocity upon the magnetic field and observe temperatures on the Doppler and sub-Doppler regime.  
We suggest several procedures for the optimization of the fountains' temperature for a wider range of magnetic fields.

## A Pound-Drever-Hall

In the upper side of figure 5 we show the schematic for the Pound-Drever-Hall locking process. A fraction of the beam enters a  $^{87}\text{Rb}$  vapor-cell after having passed through a polarizing beam splitter (PBS), it is referred to as a pump and obeys  $I_{\text{pump}} > I_{\text{sat}}$ . The pump excites atoms with velocities around the velocity that Doppler shifts the laser frequency into resonance  $v = (\omega - \omega_0)/k$ . The retro-reflected beam, referred to as a probe, is then significantly less intense than the pump obeying  $I_{\text{probe}} \ll I_{\text{sat}}$  and contrarily to the pump it interacts only with atoms with velocities  $v = (\omega + \omega_0)/k$ . The absorption profile of the probe in the absence of the pump, namely the transmission as a function of the frequency, follows a Lorentzian line-shape with a spread of the natural linewidth  $\Gamma$ . At the presence of the pump, a narrow peak appears at the atomic resonance  $\omega = \omega_0$  when two beams interact with the same atoms, of  $v = 0$ . Hence, in presence of the pump, the absorption profile has a Lorentzian, Doppler-broadened, line-shape with what is called a saturated-absorption-dip (or Lamb dip) right at  $\omega = \omega_0$ . The reason for that is that the pump beam saturates the transition for atoms around with so that around resonance absorption from the probe is very low.

In practice,  $^{87}\text{Rb}$  has three dipole transitions to which the laser fields are coupled, the  $|F = 2\rangle \leftrightarrow |F' = 1\rangle$ ,  $|F = 2\rangle \leftrightarrow |F' = 2\rangle$  and  $|F = 2\rangle \leftrightarrow |F' = 3\rangle$ , that are shown in figure 6. When the separation of two transitions is small compared to the Doppler broadening, they appear as a single broadened absorption line-shape, and the main saturated-absorption-dip is found at the middle between two transitions. These resonances are referred to as cross-over resonances and they are denoted as  $C_{nm}$  in the figure. We use this technique, referred to as saturated absorption spectroscopy [14], in order to detect the cross-over transitions. Nevertheless, if we wish to detect fluctuations in the frequency, the saturated absorption spectroscopy signal is not good enough for two main reasons. First, the signal is symmetric around resonance; hence, initially lasing on resonance, if a fluctuation in the wavelength occurs and the transmission decreases, we have no means of knowing whether the laser drifted above or below resonance. Furthermore, fluctuation in the intensity can as well result in the increase of the transmission and might be confused with wavelength fluctuations. The Pound-Drever-Hall technique [4] provides us with an error-signal that decouples fluctuations in wavelength from fluctuations in intensity as well as quantifies the lasers' drift from resonance in a manner that we can know whether it drifted above or below resonance. The technique consists on the modulation of the pump and probe. We then use the proportional-integral-derivative regulator in order to actually lock the lasers to the cross-over transitions; based on the PDH error-signal, the PID regulator restores the wavelength to resonance by slight rotations of the grating.

## B Helmholtz coils

As said in the text, when making and mounting the Helmholtz coils, an emphasis was put on lowering switching times and the magnetic field inhomogeneity in the interaction region. We tried to reduce the number of turns, in order to reduce switching times, following  $\tau \propto N$ , while not restricting ourselves to low magnetic fields. The restriction upon the magnetic fields is due to the power supply in use.

Figure 22 shows voltage measured across the Helmholtz coils. Oscillations are naturally due to the inductance of the coils, as well as to the power supply, working in current-control mode. We measure switching times on the order of  $50 \mu\text{s}$ .

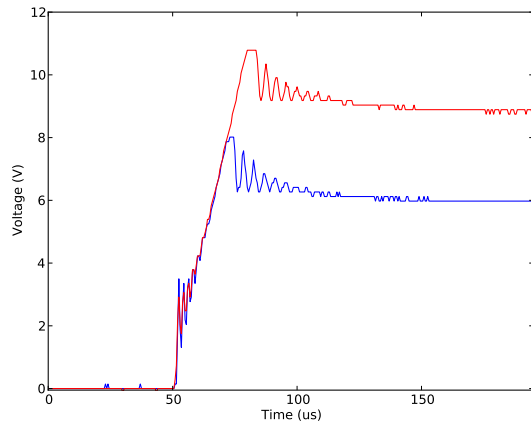


Figure 22: The voltage across the Zeeman coils as a function of time (in  $\mu s$ ). In blue is the voltage for an eventual current of 1 A and the red for 1.5 A. The switching times are measured to be about  $55 \mu s$ .

## C Experimental setup

In figures 24 and 23 we show images of the experimental setup, as it is at the end of the project.

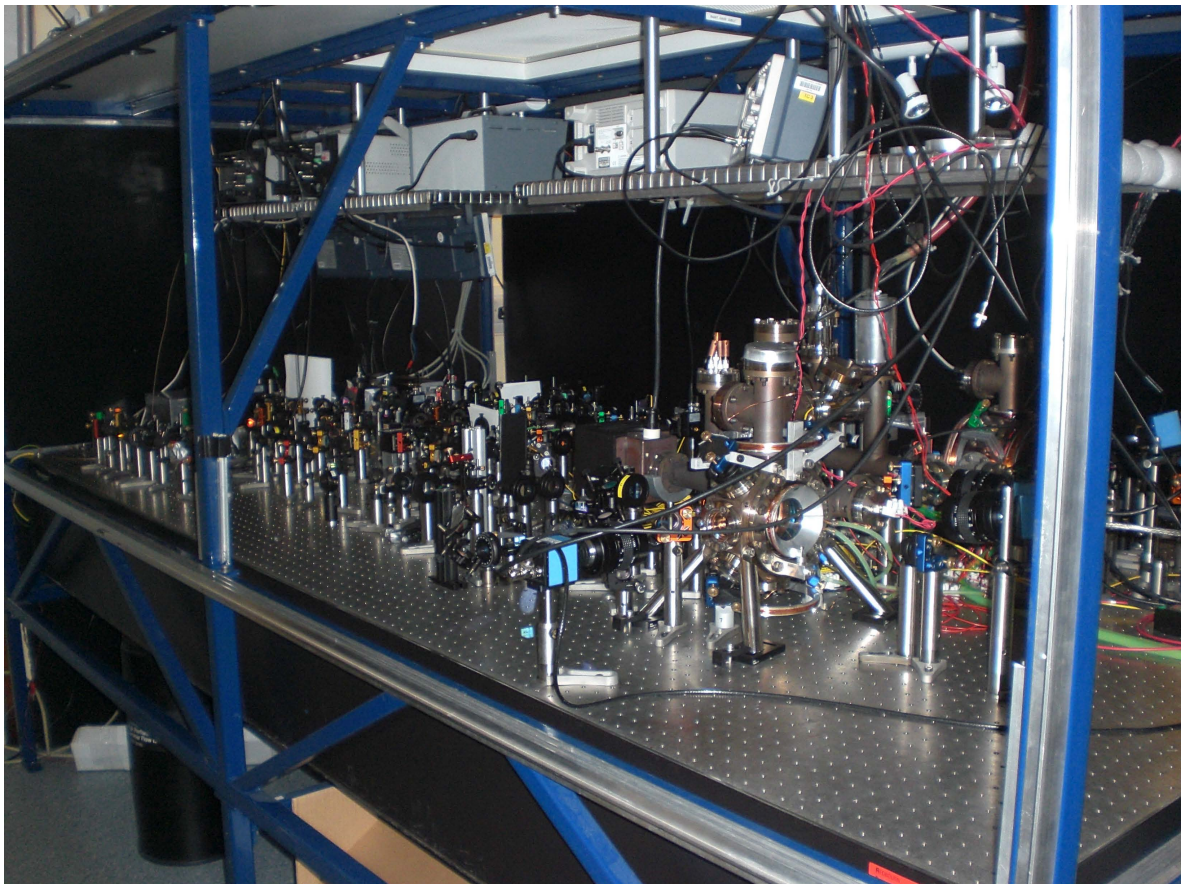


Figure 23: The experimental setup. In the back of the table are the lasers, the Fabry-Perot interferometers and the wave-length meter. Most of the beam path consists on the acousto-optical modulators, the spatial filters, the polarization manipulation and the frequency-locking instruments, an isolator, Rb vapour cells and photo-diodes. In the front we see the vacuum chamber and the two CCD cameras that we have mounted for the imaging of the MOT and the fountain.

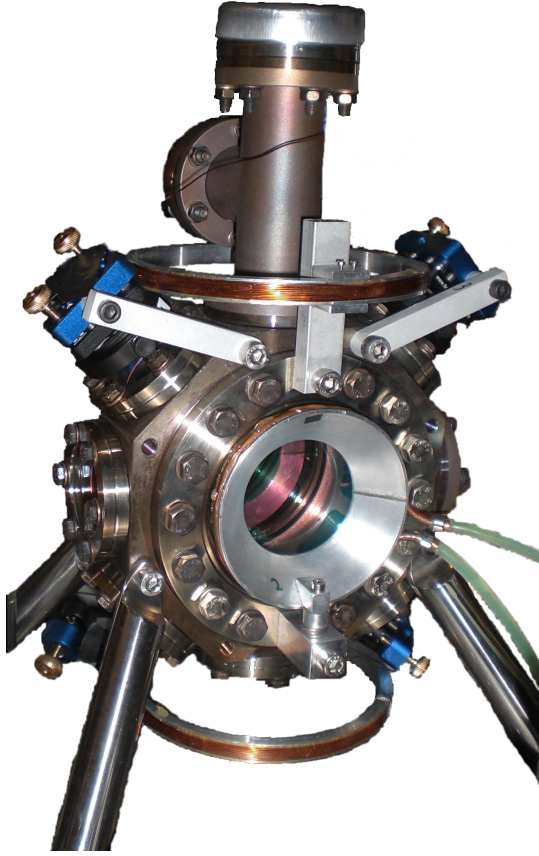


Figure 24: The vacuum chamber. In the middle is the one of the coils used to produce the MOT's magnetic field configuration. A second coil is situated in the other side of the chamber, creating together an anti-Helmholtz pair. We have remounted the anti-Helmholtz coils, now bolted-down directly to the chamber, for higher stability of the trap. Below and above the chamber we see the Helmholtz coils, producing a uniform magnetic field in the center of the chamber. We made these coils for the extraction of the atomic fountains and hence an emphasis was put on lowering switching times and the magnetic field inhomogeneity. On four sides of the chamber we see four mirrors, in blue, used for two out of three counter-propagating light fields. The two lower mirrors guide two light fields into the chamber and the two upper mirrors retro-reflect the beams for them to overlap the incident ones. Between the two upper mirrors and the vacuum chamber are  $\lambda/4$  wave plates, changing the polarization of the incident light from  $\sigma^-$  to  $\sigma^+$  in order to create the necessary polarization configuration for the MOT, and for the extraction of the fountain.

## D Numerical solution

As said in section 5.2, in order to deduce the force exerted on the atom, we must solve the time-dependent master equations describing the temporal evolution of the atom's density matrix. The time dependence arises from the motion of the atom in the space-dependent field. Namely, through the Rabi operator:

$$\hat{\Omega}(t) = \hat{\mathbf{d}} \cdot \mathbf{E}(R(t))/\hbar \quad (30)$$

where  $R(t)$  is the time-dependent atomic position.

The evolution equations for the density matrix can be expressed as follows [8]:

$$\begin{aligned} \frac{d\rho_{ee}}{dt} &= -\Gamma\rho_{ee} - iL\rho_{ee} + i\Omega\rho_{ge} - i\rho_{eg}\Omega^+, \\ \frac{d\rho_{gg}}{dt} &= \Gamma \sum_{\beta} Q_{\beta}^+ \rho_{ee} Q_{\beta} - iL\rho_{gg} + i\omega^+ \rho_{eg} - i\rho_{ge}\Omega, \\ \frac{d\rho_{eg}}{dt} &= -\left[\frac{\Gamma}{2} - i\Delta + iL\right] \rho_{eg} + i\Omega\rho_{gg} - i\rho_{ee}\Omega, \\ \frac{d\rho_{ge}}{dt} &= -\left[\frac{\Gamma}{2} + i\Delta + iL\right] \rho_{ge} + i\Omega^+ \rho_{ee} - i\rho_{gg}\Omega^+ \end{aligned} \quad (31)$$

where  $Q_{\beta}$  is the reduced dipole operator, in the complex spherical coordinates, defined by the three unit vectors  $u_{-1} = (\hat{x} - i\hat{y})/\sqrt{2}$ ,  $u_0 = \hat{z}$ ,  $u_{+1} = -(\hat{x} + i\hat{y})/\sqrt{2}$ . These unit vectors correspond to the normalised polarization vectors and are useful when considering the coupling of a light field to the atomic dipole.

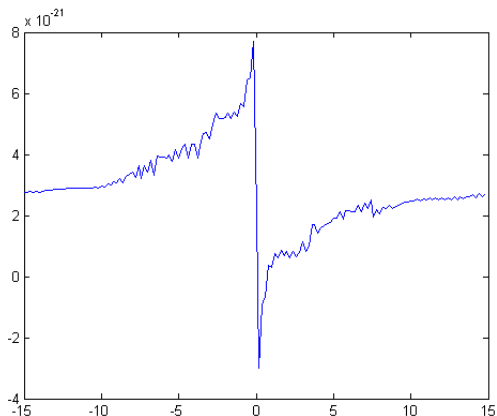


Figure 25: Force as a function of an atom's velocity. A numerical solution for a configuration of a pair of  $\sigma^+$ - $\sigma^-$  counter-propagating laser fields, perpendicular to the magnetic field. We use  $B = 5G$  and  $\Delta = -1.5\Gamma$ . The result, damping to  $v = 0$  solely, do not coincide with our expectations and experimental observations, due to (bugs) in the program.

We consider a low-intensity and low-velocity limits, where both the rate of stimulated transitions and the Doppler shift are much smaller than the natural linewidth  $\Gamma$ . The combined limits are a substantial ingredient for sub-Doppler cooling [10]. It was demonstrated [30] that when considering the Larmor frequency much smaller than the natural linewidth as well,  $\omega_L \ll \Gamma$ , the evolution equation of the sub-matrix  $\rho_{gg}$  can be deduced from equation 31 as a closed equation, after adiabatically eliminating the excited state.:

$$\frac{d}{dt}\rho_{gg} = G\rho_{gg} - (P + iS)\rho_{gg} - \rho_{gg}(P - iS) - i\omega [\mathbf{F}_g \cdot \hat{\mathbf{n}}, \rho_{gg}] \quad (32)$$

where  $G$  is the operator describing the gain of the ground-state sub-levels,  $P$  the operator describing the loss and  $\hbar S$  plays the role of an effective Hamiltonian, describing the perturbation of the energy levels due to the radiation field. All given in reference [30].

Furthermore, it was shown [37] that by a passage to the interaction representation, considering the dominant part of the Hamiltonian to be the Larmor term:

$$H_0 = \omega_L \mathbf{F}_g \cdot \hat{\mathbf{n}} \quad (33)$$

one can deduce a density matrix evolution for each velocity group  $\rho_n$ , by implementing  $\omega_L$  according to each of the three values  $|n| = 0, 1, 2$ , following equation 25. Each  $\rho_n$  applies for atoms moving close to the resonant velocity.

We programmed a Matlab code for solving these differential equations. The force was then deduced by  $F = \sum_i Tr [\hat{f}_i \cdot \hat{\rho}_i]$ , where  $\hat{f}$  is the force operator for each of the resonances, and is given in the last reference. Finally, we average on the time that an atom spends while crossing a distance of a wavelength.

In figure 25 we show an example for the numerically resolved force, for a pair of counter-propagating laser fields, perpendicular to the magnetic field, in a  $\sigma^+$ - $\sigma^-$  configuration. This configuration corresponds to the laser fields propagating along the  $y$  axis in our apparatus. A damping force with a representative line shape is clearly seen around  $v = 0$ . Nevertheless, the force did not converge to zero at both high and low velocities and we did not observe the damping to finite velocities that are to be expected. The program had apparently had several bugs in it. As the goal of the project was to mount the fountain for it to be used for the insertion of single atoms into optical cavities, efforts were put into the experimental demonstration of the fountain rather than a numerical or analytical ones.

## References

- [1] P. R. Berman. Nonlinear spectroscopy and laser cooling. *Phys. Rev. A*, 43(3):1470–1483, Feb 1991.
- [2] P. Berthoud, E. Fretel, and P. Thomann. Bright, slow, and continuous beam of laser-cooled cesium atoms. *Phys. Rev. A*, 60(6):R4241–R4244, Dec 1999.
- [3] P. Berthoud, A. Joyet, G. Duddle, N. Sagna, and P. Thomann. A continuous beam of slow, cold cesium atoms magnetically extracted from a 2d magneto-optical trap. *EPL (Europhysics Letters)*, 41(2):141, 1998.
- [4] Eric D. Black. An introduction to pound–drever–hall laser frequency stabilization. *American Journal of Physics*, 69(1):79–87, 2001.
- [5] C. Brunel, B. Lounis, P. Tamarat, and M. Orrit. Triggered source of single photons based on controlled single molecule fluorescence. *Physical Review Letters*, 83(14):2722–2725, 1999.
- [6] J. I. Cirac and P. Zoller. Quantum computations with cold trapped ions. *Phys. Rev. Lett.*, 74(20):4091–4094, May 1995.
- [7] A. Clairon, C. Salomon, S. Guellati, and W. D. Phillips. Ramsey resonance in a zacharias fountain. *EPL (Europhysics Letters)*, 16(2):165, 1991.
- [8] C. Cohen-Tannoudji. Frontiers in laser spectroscopy. *North Holland-Amsterdam*, page 1, 1991.
- [9] David G. Cory, Amr F. Fahmy, and Timothy F. Havel. Ensemble quantum computing by NMR spectroscopy. *Proceedings of the National Academy of Sciences*, 94(5):1634–1639, 1997.
- [10] J. Dalibard and C. Cohen-Tannoudji. Laser cooling below the doppler limit by polarization gradients: simple theoretical models. *J. Opt. Soc. Am. B*, 6(11):2023–2045, 1989.
- [11] F. De Martini, G. Di Giuseppe, and M. Marrocco. Single-mode generation of quantum photon states by excited single molecules in a microcavity trap. *Physical review letters*, 76(6):900–903, 1996.
- [12] D. Deutsch. Quantum Theory, the Church-Turing Principle and the Universal Quantum Computer. *Proceedings of the Royal Society of London. A. Mathematical and Physical Sciences*, 400(1818):97–117, 1985.
- [13] D. Deutsch and R. Jozsa. *ibid.*, 493:553, 1992.
- [14] Christopher J. Foot. Atomic physics. *Oxford University press*.
- [15] Y. Fukuyama, H. Kanou, V.I. Balykin, and K. Shimizu. *Appl. Phys. B: Lasers Opt.*, B70:561, 2000.
- [16] Lov K. Grover. Quantum mechanics helps in searching for a needle in a haystack. *Phys. Rev. Lett.*, 79(2):325–328, Jul 1997.
- [17] Lov K. Grover. Quantum computers can search rapidly by using almost any transformation. *Phys. Rev. Lett.*, 80(19):4329–4332, May 1998.

- [18] K. H. Kim, K. I. Lee, H. R. Noh, W. Jhe, N. Kwon, and M. Ohtsu. Cold atomic beam produced by a conical mirror funnel. *Phys. Rev. A*, 64(1):013402, May 2001.
- [19] P. Kohns, P. Buch, W. Sptitz, C. Csambal, and W. Ertmer. On-line measurement of sub-doppler temperatures in a rb magneto-optical trap-by-trap centre oscillations. *EPL (Europhysics Letters)*, 22(7):517, 1993.
- [20] A. Kuhn, M. Hennrich, and G. Rempe. Deterministic single-photon source for distributed quantum networking. *Physical review letters*, 89(6):67901, 2002.
- [21] A. Kuhn and D. Ljunggren. Cavity-based single-photon sources. *Contemporary Physics*, 51(4):289–313, July 2010.
- [22] J. R. Kuklinski, U. Gaubatz, F. T. Hioe, and K. Bergmann. Adiabatic population transfer in a three-level system driven by delayed laser pulses. *Phys. Rev. A*, 40(11):6741–6744, Dec 1989.
- [23] V. S. Letokhov and V. G. Minogin. Laser radiation pressure on free atoms. *Physics Reports*, 73(1):1 – 65, 1981.
- [24] B. Lounis and WE Moerner. Single photons on demand from a single molecule at room temperature. *Nature*, 407(6803):491–493, 2000.
- [25] Z. T. Lu, K. L. Corwin, M. J. Renn, M. H. Anderson, E. A. Cornell, and C. E. Wieman. Low-velocity intense source of atoms from a magneto-optical trap. *Phys. Rev. Lett.*, 77(16):3331–3334, Oct 1996.
- [26] H. J. Metcalf and P. van der Straten. Laser cooling and trapping.
- [27] P. Michler, A. Kiraz, C. Becher, WV Schoenfeld, PM Petroff, L. Zhang, E. Hu, and A. Imamoglu. A quantum dot single-photon turnstile device. *Science*, 290(5500):2282, 2000.
- [28] C. Monroe, W. Swann, H. Robinson, and C. Wieman. Very cold trapped atoms in a vapor cell. *Phys. Rev. Lett.*, 65(13):1571–1574, Sep 1990.
- [29] J. E. Mooij, T. P. Orlando, L. Levitov, Lin Tian, Caspar H. van der Wal, and Seth Lloyd. Josephson Persistent-Current Qubit. *Science*, 285(5430):1036–1039, 1999.
- [30] G. Nienhuis, P. van der Straten, and S-Q. Shang. Operator description of laser cooling below the doppler limit. *Phys. Rev. A*, 44(1):462–474, Jul 1991.
- [31] E.M. Purcell. Spontaneous emission probabilities at radio frequencies. *Phys. Rev.*, 69:681, 1946.
- [32] C. Salomon, J. Dalibard, W. D. Phillips, A. Clairon, and S. Guellati. Laser cooling of cesium atoms below 3 k. *EPL (Europhysics Letters)*, 12(8):683, 1990.
- [33] C. Santori, M. Pelton, G. Solomon, Y. Dale, and Y. Yamamoto. Triggered single photons from a quantum dot. *Physical Review Letters*, 86(8):1502–1505, 2001.
- [34] S-Q. Shang, B. Sheehy, H. Metcalf, P. van der Straten, and G. Nienhuis. Velocity-selective resonances and sub-doppler laser cooling. *Phys. Rev. Lett.*, 67(9):1094–1097, Aug 1991.
- [35] P. W. Shor. *Proceedings of the 35<sup>th</sup> Annual Symposium on Foundation of Computer Science (IEEE Computer Society, Los Alamos, CA, 1994)*, page 124.

- [36] C. G. Townsend, N. H. Edwards, C. J. Cooper, K. P. Zetie, C. J. Foot, A. M. Steane, P. Szriftgiser, H. Perrin, and J. Dalibard. Phase-space density in the magneto-optical trap. *Phys. Rev. A*, 52(2):1423–1440, Aug 1995.
- [37] P. van der Straten, S-Q. Shang, B. Sheehy, H. Metcalf, and G. Nienhuis. Laser cooling at low intensity in a strong magnetic field. *Phys. Rev. A*, 47(5):4160–4175, May 1993.
- [38] N. G. van Kampen. Stochastic processes in physics and chemistry. *North Holland-Amsterdam*, 1981.
- [39] C. D. Wallace, T. P. Dinneen, K. Y. N. Tan, A. Kumarakrishnan, P. L. Gould, and J. Javanainen. Measurements of temperature and spring constant in a magneto-optical trap. *J. Opt. Soc. Am. B*, 11(5):703–711, 1994.
- [40] S. Weyers, E. Aucouturier, C. Valentin, and N. Dimarcq. A continuous beam of cold cesium atoms extracted from a two-dimensional magneto-optical trap. *Optics Communications*, 143(1-3):30–34, 1997.
- [41] D. J. Wineland and Wayne M. Itano. Laser cooling of atoms. *Phys. Rev. A*, 20(4):1521–1540, Oct 1979.
- [42] V. Zwiller, H. Blom, P. Jonsson, N. Panev, S. Jeppesen, T. Tsegaye, E. Goobar, M.E. Pistol, L. Samuelson, and G. Björk. Single quantum dots emit single photons at a time: Antibunching experiments. *Applied Physics Letters*, 78:2476, 2001.